UNIVERSITY OF HELSINKI

Profiling of Spatial Tumor Microenvironment Architecture in Highly Multiplexed Images of High-Grade Serous Ovarian Carcinoma

Master's Programme in Translational Medicine,
Translational Research Study Track
Master's thesis

Author:
Alva Grönholm

Supervisor(s):
MD PhD Anniina Färkkilä
MSc Ada Junquera Mencía

7.5.2025
Helsinki

Faculty: Faculty of Medicine
Degree programme: Translational Medicine
Study track: Translational Research
Author: Alva Grönholm
Title: Profiling of Spatial Tumor Microenvironment Architecture in Highly Multiplexed Images of High-Grade Serous Ovarian Carcinoma
Level: Master's thesis
Month and year: 05.2025
Number of pages: 62
Keywords: High-grade serous ovarian carcinoma, tumor microenvironment, tCycIF, spatial analysis, spatial count, LDA, recurrent cellular neighborhood
Supervisor or supervisors: Anniina Färkkilä, Ada Junquera Mencía
Where deposited: E-thesis, University of Helsinki

Abstract:

High-grade serous ovarian carcinoma (HGSC) is the most lethal subtype of ovarian cancer, characterized by genomic instability, late diagnosis and high rates of recurrence. The tumor microenvironment (TME) plays a critical role in disease progression and treatment resistance, with its spatial organization offering potential insights into therapeutic outcomes. Advances in highly multiplexed imaging and computational analysis have enabled deeper characterization of the TME, yet optimal strategies for analyzing the TME architecture remain to be explored.

This thesis investigates the spatial organization of the TME in chemotherapy-treated HGSC patients by applying two spatial analysis methods, spatial count and Latent Dirichlet Allocation (LDA), to tissue cyclic immunofluorescence (tCycIF) imaging data. By analyzing recurrent cellular neighborhoods (RCNs) across multiple spatial scales, the ability of each method to detect spatial patterns and their clinical relevance is assessed.

The analysis reveals interpatient heterogeneity in the HGSC TME, with distinct immune, stromal, and tumor composition. Spatial count effectively captured fine-grained, localized structures but showed sensitivity to spatial scale. In contrast, LDA identified subtle spatial patterns and remained more stable across radii. Notably, stromal-enriched RCNs were more abundant in patients with shorter progression-free survival (PFS), suggesting a link between spatial architecture and clinical outcome.

In conclusion, spatial profiling provides valuable insights into the spatial organization of the TME and its prognostic significance. Spatial count and LDA offer complementary strengths, and the choice of method and spatial resolution should be guided by the specific biological question. These results emphasize the importance of integrating spatial analysis into HGSC research and highlight its potential for improving patient stratification and tailoring treatment strategies.

Table of contents

List of Abbreviations

CAF	Cancer-associated fibroblast
DC	Dendritic cell
FFPE	Formalin-fixed paraffin-embedded
HGSC	High-grade serous carcinoma
HR	Homologous recombination
HRD	Homologous recombination deficiency
HRP	Homologous recombination proficiency
IDS	Interval debulking surgery
IL	Interleukin
INF-y	Interferon gamma
LDA	Latent Dirichlet Allocation
MHC	Major histocompatibility complex
NACT	Neoadjuvant chemotherapy
NK cell	Natural killer cell
PARP	Poly (ADP-ribose) polymerase
PDS	Primary debulking surgery
PFS	Progression-free survival
RCN	Recurrent cellular neighborhood
TAM	Tumor-associated macrophage
TCR	T cell receptor
tCycIF	Tissue-based cyclic immunofluorescence
TIL	Tumor-infiltrating lymphocyte
TIME	Tumor immune microenvironment
TLS	Tertiary lymphoid structure
TME	Tumor microenvironment
Treg	Regulatory T cell
TSI	Tumor-stroma interface
VEGF	Vascular endothelial growth factor

1 Literature review

1.1 High-grade serous ovarian carcinoma

Ovarian cancer is the third most prevalent gynecological cancer, known for its poor prognosis and high mortality rate. The high mortality rate is affected by the delayed diagnosis influenced by the late onset of symptoms, the tumor's asymptomatic growth, insufficient screening methods as well as the absence of reliable biomarkers for early detection (Momenimovahed et al., 2019). Globally, ovarian cancer is the 7th most common cancer and the 8th leading cause of cancer-related deaths in women (Lisio et al., 2019). In Finland, around 500 women are diagnosed with ovarian cancer annually, with a five-year survival rate of 48% (*Munasarjasyöpä*, n.d.).

Ovarian cancer is a highly heterogeneous disease, classified into two main types: type I and type II tumors. Type I tumors are typically low-grade, genetically stable and associated with favorable clinical outcomes. In contrast, type II tumors are high-grade, genetically unstable and progress rapidly accounting for 90% of ovarian cancer deaths (Kurman & Shih, 2016).

Among type II tumors, high-grade serous carcinoma (HGSC) is the most prevalent and lethal subtype of all ovarian cancer (Momenimovahed et al., 2019). HGSC is thought to originate in the secretory cells of the fallopian tube, enabling it to spread easily into the peritoneum due to the lack of anatomical barriers (Bowtell et al., 2015). HGSC is often diagnosed at advanced stages, such as FIGO stage III, when the disease has spread beyond the pelvis into the peritoneal cavity, or stage IV, when the disease has spread beyond the peritoneal cavity (Matulonis et al., 2016; Momenimovahed et al., 2019).

The incidence of HGSC increases in women over the age of 65, with the median age at diagnosis ranging from 50 to 79 years (Momenimovahed et al., 2019). Symptoms of HGSC are often vague and non-specific, including abdominal pain, nausea, bloating, and fatigue (Lisio et al., 2019). Risk factors for HGSC include lifetime ovulation cycles and the presence of germline mutations in the BRCA gene (Kurman & Shih, 2016).

HGSC is characterized by genomic instability, with most tumors harboring TP53 mutations. Approximately 50% of HGSC cases exhibit defects in the homologous recombination (HR) repair pathway, including BRCA1/2 mutations, which are found

in around 20% of patients ('Integrated Genomic Analyses of Ovarian Carcinoma', 2011). In addition to BRCA1/2, other genes such as PTEN, RAD51C, ATM and ATR can also be affected in the HR repair pathway in HGSC (Lisio et al., 2019). The HR repair pathway is an efficient and accurate DNA repair mechanism that relies on undamaged sister chromatid DNA. In contrast, the non-homologous end-joining (NHEJ) pathway does not require a template, often resulting in the introduction of errors (O'Connor, 2015). Based on the tumors HR status, patients can be divided into two main groups: those with a proficient HR repair pathway (HRP) and those with a deficiency in the HR repair pathway (HRD) (Lorusso et al., 2020). HRD tumors rely on alternative forms of DNA repair, such as NHEJ, which leads to a significant increase in genomic instability. This heightened instability can result in unsustainable replication and, ultimately, cell death (O'Connor, 2015). Although the molecular landscape of HGSC tumors shares similarities, significant inter- and intra-tumoral differences highlight the heterogeneity of HGSC and the need for diverse treatment approaches among patients (Roberts et al., 2019).

1.1.1 Standard treatment approaches for HGSC

The first-line treatment for HGSC is primary debulking surgery (PDS) followed by adjuvant chemotherapy. Standard adjuvant chemotherapy consists of six rounds of intravenous carboplatin/paclitaxel chemotherapy, administered every three weeks. For patients with advanced stages of the disease, who are not suitable candidates for PDS, three rounds of neoadjuvant chemotherapy (NACT) followed by interval debulking surgery (IDS), and an additional three rounds of adjuvant chemotherapy is the recommended option (Armstrong et al., 2021). Initially, upon diagnosis, HGSC typically responds well to chemotherapy; however, due to the development of platinum resistance, approximately 70-80% of patients will relapse within two years of completing first-line therapy (Lorusso et al., 2020; Matulonis et al., 2016).

Over the last decade, maintenance treatment for HGSC patients has gained significant attention, with the goal of extending the platinum-free interval, defined as the time between the last platinum treatment and the detection of disease recurrence (Lorusso et al., 2020; St Laurent & Liu, 2024). Based on two large-scale clinical trials, GOG 218 and ICON7, bevacizumab, an antiangiogenic drug, has become a part of the standard of care for newly diagnosed patients with advanced ovarian cancer. Bevacizumab

targets vascular endothelial growth factor (VEGF), a key driver of angiogenesis and tumor progression in ovarian cancer (Burger et al., 2012; Oza et al., 2015). Angiogenesis, the formation of new blood vessels, provides a crucial supply of oxygen, nutrients, and immune cells to cancer cells while removing waste products. This process, activated by different proteins such as VEGFs, not only supports rapid tumor growth but also plays an important role in metastatic spread (Nishida et al., 2006). To overcome the tumor's hypoxic and acidic microenvironment, the tumor activates angiogenesis to restore oxygen and nutrient delivery, while bevacizumab inhibits this process by binding to VEGF, reducing the tumor's blood supply and slowing disease progression (Anderson & Simon, 2020; Oza et al., 2015). In these clinical trials, bevacizumab was administered in addition to chemotherapy as maintenance therapy for 12 or 15 months, resulting in a significant increase in progression-free survival (PFS), which is the duration of time during and after treatment when the disease does not recur. However, despite the positive impact on PFS, bevacizumab did not have a significant benefit on the overall survival in the entire patient cohort. Nonetheless, a subgroup analysis revealed improved overall survival in poor-prognosis patients who received bevacizumab (Burger et al., 2012; Oza et al., 2015).

The approval of poly (ADP-ribose) polymerase (PARP) inhibitors represented a major breakthrough in the treatment of HGSC. This targeted therapy significantly extended the PFS for a subset of patients with deficiencies in the HR repair pathway, fundamentally changing the treatment strategy of these patients (Lorusso et al., 2020).

PARP enzymes play a crucial role in repairing single-strand DNA breaks by detecting damage and recruiting repair proteins. In HRD tumors, where the homologous recombination repair pathway is impaired, cells rely on alternative, error-prone DNA damage repair pathways for survival, a phenomenon known as synthetic lethality. (O'Connor, 2015). PARP inhibitors exploit this vulnerability by trapping PARP enzymes at single-strand break sites, preventing the repair of the DNA damage. This results in the accumulation of double-strand breaks that cannot be accurately repaired in HRD tumors, ultimately leading to apoptosis (Cordani et al., 2023; Lorusso et al., 2020). This selective mechanism allows PARP inhibitors to eliminate cancer cells while sparing normal cells, offering a significant advantage over traditional chemotherapies (O'Connor, 2015). Clinical trials in platinum-sensitive relapsed patients have shown that PARP inhibitors significantly increase the PFS, although there was no difference

in overall survival between patient cohorts (Ledermann et al., 2012; Pujade-Lauraine et al., 2017). However, the development of drug resistance remains a significant challenge with PARP inhibitors. Strategies to overcome resistance are being actively explored, with the most promising approaches involving the combination of PARP inhibitors with antiangiogenic agents and immune checkpoint inhibitors (Cordani et al., 2023). While these advances have greatly improved treatment outcomes for HRD patients, there remains a lack of effective therapeutic strategies for HRP tumors, which highlights the urgent need for further research in this field.

1.2 Tumor microenvironment

The initiation, growth, and progression of cancer are not only influenced by the action of cancer cells themselves but also by the surrounding tumor microenvironment (TME). The TME comprises a dynamic network of cancer cells, immune cells, stromal components, including blood vessels, fibroblasts, and extracellular matrix, all of which interact to shape the tumor's biological behavior (Hansen et al., 2016). This constantly evolving environment supports tumor growth and spread by suppressing the immune system, promoting angiogenesis to supply oxygen and nutrients, and altering surrounding tissues to aid invasion and metastasis (Visser & Joyce, 2023).

Immune cells within the TME play a dual role in tumor progression, acting either as anti-tumor agents or as immune-suppressive factors. These immune cells can be broadly categorized into two groups: innate and adaptive immune cells. Innate immune cells, such as macrophages, dendritic cells (DCs), neutrophils, and natural killer (NK) cells, provide a non-specific first line of defense when foreign antigens are detected. In contrast, the adaptive immune response, mediated by T cells and B cells, is activated later by specific antigens. This response also develops immunological memory, enabling a stronger and faster immune response if the same antigen is encountered in the future (Anderson & Simon, 2020; Hinshaw & Shevde, 2019).

Innate immune cells in the TME

Macrophages are key regulators of immune responses, playing essential roles in pathogen clearance, antigen presentation, and tissue repair. Depending on environmental signals, monocyte-derived macrophages can differentiate into distinct functional states: inflammatory M1 macrophages, which are primarily involved in

pathogen clearance and cytotoxic activity, and immune-suppressive M2 macrophages, which support tissue regeneration and wound healing (Anderson & Simon, 2020). Recent findings suggest that macrophage polarization is not limited to a strict M1/M2 classification but rather exists along a dynamic spectrum of differentiation (Xue et al., 2014). Tumor-associated macrophages (TAMs), which are among the most abundant immune cells in ovarian cancer, play a crucial role in tumor development, invasion and metastasis. M1 macrophages, characterized by high interleukin-12 (IL-12), IL-23 and low IL-10, are effective eliminators of tumor cells. In contrast, M2 macrophages, which produce high levels of IL-10 and lower levels of IL-12 and IL-13, promote angiogenesis and tissue remodeling, thereby supporting tumor growth (Yin et al., 2019).

DCs are another type of myeloid cells, critical for the activation of T cells. They recognize, capture and present antigens to T cells, serving as a critical bridge between the innate and adaptive immune response. While DCs inherently possess anti-tumorigenic properties, tumors exploit them by secreting immunosuppressive cytokines that make DC's tolerate the presence of tumor cells, leading to no activation of T cells and thereby allowing tumor persistence (Anderson & Simon, 2020).

Adaptive immune cells in the TME

Tumor-infiltrating lymphocytes (TILs) consist of T cells and B cells, which are localized in the tumor stroma or the intraepithelium (Santoiemma & Powell, 2015). These immune cells play critical roles in tumor surveillance and elimination, but their functions can be modulated by the TME.

T cells have unique T cell receptors (TCRs) that recognize specific antigens and can be divided into subsets, such as CD8+ and CD4+ T cells, each of which influences tumorigenesis in its own way. CD8+ T cells become activated when their TCRs recognize tumor antigens presented on major histocompatibility complex (MHC) I molecules by antigen-presenting cells. Once activated, they play a critical role in tumor surveillance by detecting the same antigens presented on MHC class I molecules of tumor cells and inducing cell death through cytotoxic mechanisms such as perforin or FAS-dependent pathways (Anderson & Simon, 2020; Dhatchinamoorthy et al., 2021). In addition, CD8+ T cells also suppress angiogenesis by secreting interferon gamma (INF-y), a cytokine that also promotes local inflammation to further eliminate tumor cells. This immune-mediated targeting of tumor cells is part of a broader process

known as cancer immunoediting, which includes three phases. In the elimination phase, immune cells recognize and destroy tumor cells. However, not all tumor cells are eradicated during this phase and some surviving cells enter the equilibrium phase, where a balance is maintained between anti-tumoral immune responses and tumor growth. Over time, mutations in the surviving cells may allow them to evade immune recognition and destruction, leading to the escape phase. During this phase, the tumor resumes uncontrolled growth and fully evades the immune system (Santoiemma & Powell, 2015).

Despite their central role in tumor elimination, CD8+ T cells often become dysfunctional in the TME due to chronic antigen exposure and immune suppression. This leads to T cell exhaustion, a state characterized by impaired effector functions and the upregulation of inhibitory immune checkpoint molecules such as programmed cell death-1 (PD-1), cytotoxic T-lymphocyte-associated antigen 4 (CTLA-4), lymphocyte activation gene-3 (LAG-3), and T cell immunoglobulin and mucin-domain-containing protein-3 (TIM-3). These exhausted T cells lose their cytotoxic capacity, allowing tumor cells to persist (Drakes & Stiff, 2018; Saleh & Elkord, 2020b). Notably, TIM-3 is highly expressed on CD8+ and CD4+ T cells, DCs, regulatory T cells (Tregs), and NK cells in ovarian cancer (Kabala et al., 2023). Its interaction with galectin-9 promotes T cell apoptosis and is associated with disease severity and more advanced FIGO stages (III-IV). Therapeutic inhibition of TIM-3 may help restore T cell function and overcome Treg-mediated suppression (Xu et al., 2017).

CD4+ T cells are involved in a variety of immune responses and differentiate into various subtypes. They play a crucial role in adaptive immunity, responding to antigens presented by MHC class II molecules on antigen-presenting cells. Their differentiation into distinct subsets is shaped by cytokines, antigens, and other environmental signals, enabling specialized immune functions (Speiser et al., 2023). A subtype of CD4+ T cells, T helper 1 cells are proinflammatory and support CD8+ T cells by secreting IL-2 and INF-y, promoting their expansion, migration and cytotoxic activity (Anderson & Simon, 2020). Additionally, CD4+ T cells enhance anti-tumor responses by activating antigen-presenting cells and further amplifying immune signaling in the TME (Speiser et al., 2023).

FOXP3+ CD4+ T cells, or Tregs, are a subset of CD4+ T cells, with immunosuppressive functions, defined by the expression of the Forkhead box protein P3 (FOXP3)

transcription factor. Under normal conditions, Tregs play an important protective role in maintaining immune homeostasis. However, within the TME, Tregs contribute to an immunosuppressive environment and are associated with poor prognosis. Specifically, Tregs suppress the activity of T cells, macrophages and NK cells by increasing cytokines levels and inhibitory immune checkpoints, leading to apoptosis and inhibition of proliferation (Saleh & Elkord, 2020b). Additionally, Tregs interact with TAMs, enhancing the accumulation of immunosuppressive cells and promoting pro-tumor effects in the TME. Tregs have also been shown to play a significant role in the development of resistance to immunotherapies (Saleh & Elkord, 2020a). High levels of Tregs in ovarian tumor tissue are linked to disease progression and reduced survival, making Tregs a negative prognostic factor for ovarian cancer patients (Curiel et al., 2004).

B cells are typically less abundant in the TME compared to T cells, but they still play important roles, including antibody production, antigen presentation and cytokine secretion. In the TME, B cells are important for the formation of tertiary lymphoid structures (TLS), which enables crucial interactions between T and B cells (Sharonov et al., 2020). In ovarian cancer the presence of TLSs has been associated with favorable outcomes (Kroeger et al., 2016). While B cells can exert anti-tumoral effects through tumor-specific antibody production and tumor antigen presentation to T cells, certain subsets may also promote immunosuppressive effects (Sharonov et al., 2020).

Non-immune components of the TME

Beyond immune cells, the TME consists of endothelial cells, stromal cells as well as extracellular matrix. These non-malignant cells have an important role in tumor growth, metastasis, metabolism and immune evasion (Zhao et al., 2023).

Cancer-associated fibroblasts (CAFs) are a common subtype within the tumor stroma and often arise from normal fibroblasts in response to various signaling factors, such as transforming growth factor-β and Fibroblast Growth Factor-2 secreted by tumor cells. The majority of CAFs are tumor-promoting, secreting factors that play a crucial role in immune evasion, support tumor growth and enhance the migration and invasion of cancer cells (Zhao et al., 2023). In ovarian cancer, an increased abundance of CAFs has been linked to advanced disease stages and higher incidence of omental metastases (Zhang et al., 2011).

Endothelial cells line blood vessels and are crucial for blood vessel formation, nutrient delivery and immune cell transport. In tumors, as they grow and become hypoxic, endothelial cells are activated to promote angiogenesis by secreting factors like VEGF. These newly formed vessels are often immature and leaky, allowing tumor cells to pass through the vessel walls and enter the bloodstream, enabling their spread to other organs (Anderson & Simon, 2020).

Tumor cells within the TME frequently escape immune detection by forming physical barriers that obstruct the infiltration of immune cells into the tumor. This protective strategy is primarily driven by alterations in the TME which are influenced by immune and stromal cells as well as changes in the structure of the extracellular matrix (Galassi et al., 2024). The spatial arrangement of these components plays a critical role in understanding how tumors evade immune detection and resist therapeutic interventions. Further exploring the spatial organization of the TME is key to understanding how tumors respond to treatment and why certain therapies fail (Launonen et al., 2024).

1.3 Spatial exploration of the TME

Despite the immunogenic nature of HGSC, clinical trials of immune checkpoint inhibitors have shown limited success, and no immunotherapeutic agent has received regulatory approval (Ghisoni et al., 2024). To better understand why immunotherapy responses vary, it is crucial to study the spatial organization of the TME, as cell arrangements influence microenvironmental niches, nutrient distribution and cell-cell interactions that shape tumor behavior and therapeutic response (Elhanani et al., 2023).

As mentioned previously, the TME is a complex network of cellular and acellular components that together regulate tumor growth, invasion, metastasis and response to treatments. It has been shown that good and poor responders to NACT in HGSC exhibit distinct TME compositions. For instance, stromal components, particularly mesenchymal-derived cells, are enriched in poor-responders, where they may contribute to resistance by maintaining communication between immune and epithelial cells, thereby aiding tumor survival during treatment. Interestingly, in poor responders, mesenchymal cells were found in close proximity to tumor cells, whereas

in good responders, tumor cells were more closely associated with immune cells (Stur et al., 2022).

The immune landscape within the tumor microenvironment can be categorized into three types based on the degree of TIL infiltration: immune infiltrated, immune excluded and immune silent. Immune infiltrated tumors exhibit widespread immune cell distribution across the tumor, indicating a strong immune response. In contrast, immune excluded tumors typically have T cells confined to the outer edges of the tumor, with little to no penetration into the tumor microenvironment. Finally immune silent tumors lack the presence of immune cells altogether, indicating an absence of immune response (Anderson & Simon, 2020).

In HGSC patients the presence of CD8+ T cells within the TME has been associated with a favorable prognosis and an increase in overall survival. Although CD8+ T cells have been associated with improved survival, the location of these cells within the TME is crucial. CD8+ T cells located within the intraepithelial region are correlated with better survival outcomes, whereas stromal CD8+ T cells show no significant prognostic impact (Sato et al., 2005).

Additionally, recent studies show that the spatial organization of myeloid cells play a critical role in immune responses. Specifically, both M1- and M2-polarized macrophages form spatial clusters, contributing to T cell exhaustion especially in chemotherapy-exposed tumors (Launonen et al., 2024).

Furthermore, the TME differs between molecular subtypes of HGSC, particularly in relation to HR status. BRCA1/2-mutated tumors exhibit increased immune infiltration, with greater proximity between T cells and proliferating tumor cells, suggesting enhanced immunosurveillance. In contrast, HRP tumors are characterized by lower T cell infiltration and higher stromal content, with immune cells often localized in distinct regions, which may limit their interactions with tumor cells (Launonen et al., 2022).

These spatial differences play a critical role in treatment responses and disease progression, emphasizing the need for advanced spatial profiling techniques to refine patient stratification and guide therapeutic strategies.

1.3.1 Tools for analyzing the spatial TME

In recent years, new technological advancements have been made for studying the spatial architecture of the TME. Various methods now enable the analysis of multiple proteins and transcripts in tissue samples while preserving the spatial organization. These techniques range from microscopy-based proteomic techniques, which use antibodies labelled with fluorophores, enzymes, or DNA oligos, to mass spectrometry-based methods that offer high-resolution, high-plex imaging (Elhanani et al., 2023).

One prominent method is tissue-based cyclic immunofluorescence (tCycIF), a highly multiplexed imaging technique that uses iterative rounds of staining, imaging, and bleaching to analyze formalin-fixed paraffin-embedded (FFPE) samples. This allows for the detection of up to 60 different proteins, providing deep insights into protein expression patterns, cellular interactions and functional characteristics within the TME (Lin et al., 2018). Compared to some other multiplexed immunohistochemistry methods, which can stain for up to 12 proteins, tCycIF significantly increases the number of proteins analyzed per sample (Lin et al., 2018; Tsujikawa et al., 2017).

To reduce imaging time, CODEX uses primary antibodies labelled with unique DNA oligos, enabling a single antibody hybridization followed by shorter cycles of labelling, imaging and signal removal (Goltsev et al., 2018). MIBI on the other hand uses antibodies labelled with metal isotopes and mass spectrometry for protein detection at subcellular resolution (Angelo et al., 2014). While this approach eliminates spectral overlap, it is destructive to the tissue and has lower imaging throughput compared to tCycIF.

Additionally, tCycIF allows multiscale imaging, from whole-tissue architecture down to subcellular details, and is compatible with conventional histopathology methods like H&E staining, making it an adaptable tool for both research and clinical applications. Given the strengths and limitations of each approach, hybrid methods combining tCycIF with techniques like CODEX or MIBI may ultimately provide the most comprehensive spatial proteomic analysis (Lin et al., 2018).

1.3.2 Spatial profiling of the TME

Multiplexed imaging techniques offer a detailed view of the complex molecular landscape and spatial organization of solid tumors. These methods generate extensive

datasets that capture various layers of information, including single-cell phenotypes, morphology, cell composition, cellular interactions and the structural organization of the TME. Extraction of these single-cell features includes cell segmentation, generating a protein expression matrix, and identifying phenotypes using either manual gating techniques or classification algorithms (Elhanani et al., 2023).

These approaches reveal the cellular composition of the TME, highlighting the distribution of tumor, immune, and stromal cells (Elhanani et al., 2023). Spatial profiling allows for further focus not only on cell composition but also on the physical location of cell types. The spatial organization can be analyzed at both a close range, focusing on cell-to-cell interactions or at a larger scale focusing on microenvironments within the TME. For example, the proximity of immune cells to tumor cells can indicate their potential to eliminate tumor cells or, conversely, how tumor cells evade immune responses. Studying the TME on a larger scale, structures such as TLSs can be identified, which are associated with antitumor immune responses and improved clinical outcomes in several cancers. Overall, while cell-to-cell interactions are essential for understanding the complexity of the TME, larger structures highlight the spatial organization of cells and their potential impact on immune response and clinical outcomes. Computational approaches enable the identification of TME structures that are undetectable to the human eye (T. Fu et al., 2021).

Several computational approaches exist for detecting recurrent cellular neighborhoods (RCNs), which are spatially recurring patterns of cell organization that may reveal functionally significant microenvironments in the TME. For instance, RCNs can be identified using a predefined radius, where each single cell's neighborhood is determined based on the presence of surrounding cells within that radius. By clustering the computed neighborhood matrix, RCNs representing frequently occurring cellular structures in the TME can be identified (Launonen et al., 2024; Nirmal & Sorger, 2024).

Another approach is Latent Dirichlet Allocation (LDA), a probabilistic modeling method used to uncover latent spatial motifs in cellular distribution. For instance, LDA can be trained with a neighborhood matrix based on a predefined radius and, through an iterative refinement process, probabilistically assign each cell to latent motifs while updating these assignments based on learned spatial dependencies. This process generates probability distributions that describe spatial organization, representing

each cell as a mixture of recurrent spatial motifs (Chen et al., 2020; Nirmal et al., 2022). LDA has been widely applied in biodiversity studies, as it can detect both gradual and sudden shifts in the composition and organization of biological communities, such as animal populations in a habitat or cells in a tissue (Nirmal et al., 2022). In the TME, it has been used to capture spatial transitions in cellular neighborhoods. Additionally, adjusting the number of motifs allows for different levels of granularity, from large-scale regions to finer structures, revealing subtle differences within and between cell types (Chen et al., 2020).

By integrating spatial analysis data with clinical and patient data, the function and clinical implications of these discovered RCNs can be uncovered (Elhanani et al., 2023). For instance, in HGSC, differences in the TME between BRCA mutants and HR wildtype patients were discovered computing RCN with a predefined radius (Launonen et al., 2022). Furthermore, in a melanoma study, LDA revealed that the most significant shift in RCNs occurred between precursor lesions and melanoma in situ, where the immune environment became more immunosuppressive and spatially structured, forming a barrier that excluded TILs. (Nirmal et al., 2022).

Several challenges also arise, including limitations in throughput, time, and potential biases. Studying the TME requires large cohorts to accurately capture inter- and intra-tumoral heterogeneity. However, many spatial profiling techniques are relatively new, often restricted by limited throughput or high cost, which can reduce cohort sizes. Time is another critical factor, as processes such as probe design, antibody validations and sample preparation can be labor-intensive. Additionally, imaging time increases with sample number and the size of the scanned area, limiting scalability. Finally, biopsy size may introduce bias, as small tissue samples might not fully capture the complexity of the heterogenous TME, possibly overlooking key aspects of the TME (Elhanani et al., 2023).

As spatial profiling techniques continue to evolve, new opportunities are emerging to deepen the understanding of the TME. One potential prospective would be integrating spatial profiling with the field of artificial intelligence (Elhanani et al., 2023). AI-driven analysis of histopathological features in H&E have already been shown to identify molecular alterations and improve diagnostic accuracy (Y. Fu et al., 2020). Additionally, the development of 3D spatial profiling techniques could provide a more comprehensive understanding of the TME, allowing them to capture the full

complexity of cellular interactions and tumor progression compared to 2D imaging. With continued innovation, spatial profiling has potential to refine therapeutic approaches, guide the development of novel treatments and improve clinical decision-making for cancer patients (Toninelli et al., 2023).

2 Aims and objectives

This study aims to investigate the TME in chemo-treated HGSC patients by integrating tCycIF imaging and clinical data from the ongoing Oncosys-OVA prospective clinical trial. By comparing two spatial analysis methods, spatial count and LDA, the study seeks to analyze RCNs at varying spatial scales and evaluate how each method captures the TME's complexity and identifies clinically relevant spatial patterns across patient groups. The objectives are as follows.

1. **Phenotypic labeling:** Assign phenotype labels to single-cell data obtained from tCycIF imaging to identify and classify tumor, stromal, endothelial, and immune cell populations within the TME.

2. **Composition analysis:** Examine the cellular composition of the TME, identifying key cell types and their distributions across patients.

3. **Compute recurrent cellular neighborhoods:** Compute RCNs using spatial count and LDA at three spatial scales (13, 25, and 35 microns), assessing how each method captures and defines RCNs.

4. **Methodological evaluation:** Compare the RCNs derived from spatial count and LDA, analyzing the impact of spatial scale on the results and how each method responds to different radii.

5. **Clinical comparison:** Compare RCNs derived from LDA and spatial count across distinct clinical groups to evaluate each method's ability to detect clinically relevant spatial patterns.

3 Material and methods

3.1 Material

3.1.1 Cohort description

The cohort data was obtained from participants in the prospective ONCOSYS-OVA (NCT06117384) clinical trial conducted at Helsinki University Hospital and the University of Helsinki. In this cohort, samples were collected from HR-proficient HGSC patients, treated with adjuvant chemotherapy and IDS for FIGO stage IIIC-IVB tumors.

A total of 19 samples were selected based on specific criteria, including a PFS of more than six months and a tumor purity of at least 10-15%, as assessed by an expert pathologist (Fig. 1a). Of these, 18 were omental samples, and one was a tubular sample.

Formalin-fixed paraffin embedded (FFPE) tissue blocks, along with surgical and clinical data, were collected. Extracted clinical data included patient age, tumor histology, FIGO stage, primary tumor site, and residual disease status after surgery. Additionally, data on treatment regimens, progression-free survival (PFS), BRCA 1/2 mutational status, and homologous recombination deficiency (HRD) status were obtained. Genomic analyses included BRCA1/2 mutational analysis and genomic scarring assessment (ovaHRDscar). PFS was defined as the time from diagnosis to the date of progression. Patients were classified into three categories based on their PFS: short PFS (below the 33rd percentile), long PFS (above the 66th percentile), and intermediate PFS (between the 33rd and 66th percentiles).

The study has been approved by the ethics committees of the Women's Clinic at Helsinki University Hospital (HUH) and Helsinki Biobank. Patient identifiers and personal information in the clinical data are stored securely on the HUH server using the HUH Datalake at Helsinki Biobank, with access strictly limited to authorized personnel. In publicly available datasets, each patient is assigned a unique, randomized ID to ensure complete anonymity and prevent any risk of identification.

3.2 Methods

3.2.1 tCycIF imaging and image processing

Performed by laboratory colleagues

FFPE tissue blocks were sectioned into 5 μm thick tissue sections and stained with a validated antibody panel targeting 36 protein markers to identify cell types and functional states (Supplementary Table 1). Following the tCyCIF protocol (Lin et al., 2018), the slides were scanned using a RareCyte CyteFinder scanner. Image processing was performed with ASHLAR (Alignment by Simultaneous Harmonization of Layer/Adjacency Registration), an open-source Python tool that performs both stitching, aligning adjacent tiles within each cycle, and registration, aligning tiles from different cycles covering the same regions (Muhlich et al., 2022).

Next, single cell segmentation was carried out using STARDIST which detects nuclei in fluorescent images based on the Hoechst channel (Weigert et al., 2020). Quantification of single-cell level information was then performed using the scikit-image Python package, generating a dataset with parameters for spatial analysis, including CellID, spatial coordinates, eccentricity, area and marker intensity values. Furthermore, quality control of images was conducted in Cylinter, removing any areas with artifacts from downstream analysis (Baker et al., 2024).

3.2.2 tCycIF image data processing

Data normalization

The single-cell marker intensity data was normalized using the pp.log1p function in Scimap, which applies a log1p transformation to the data (Nirmal & Sorger, 2024).

Marker gating

Cell type annotation markers were manually gated using Scimap (Nirmal & Sorger, 2024). Gating was performed with pl.gate_finder in Scimap, which uses Napari to visualize OME-TIFF images. During this process, marker channels with different gates were manually inspected by overlaying the gates on top of the marker in question, and the threshold is set based on the most accurate representation of positive cells.

Phenotyping

Cell type annotations for the single-cell dataset was performed using the tl.phenotype_cells function in Scimap (Nirmal & Sorger, 2024). A total of 15 markers were used to annotate 12 distinct phenotypes (Fig. 1b). Prior to phenotyping, the data was scaled using the tl.rescale function based on the defined gates from the previous step, and a predefined, sample-specific phenotype logic table was constructed (Fig. 1c).

Each logic table was sample specific, but the phenotyping approach followed three main steps: (1) separating tumor cells from the rest of cells, such as stromal and immune, (2) identification of stromal, lymphoid and myeloid cells, and (3) further classifying each group into subtypes. Stromal cells were defined by positivity for αSMA, Vimentin, or FAP, with endothelial cells identified as CD31+. Lymphoid cells were categorized as CD4+ T cells (CD4+), CD8+ T cells (CD8+), FOXP3+ regulatory T cells (FOXP3+ and CD4+), B cells (CD20+), and NK cells (NKG2A+). Myeloid cells were further classified into DCs expressing CD11c, CD163+ DCs co-expressing CD11c and CD163, CD163- macrophages identified as IBA1+ CD163-, and CD163+ macrophages as IBA1+ CD163+.

To ensure phenotyping accuracy, image verification for each sample was performed using the pl.image_viewer function in Scimap-toolkit. Phenotype masks were overlaid on the tCyCIF images, and the assigned phenotypes were visually inspected to confirm that the cells expressed the expected markers (Fig. 1d). The logic table was iteratively adjusted and rechecked for each sample until the phenotyping was visually accurate.

Cells that did not fully meet the criteria for a specific phenotype were initially labelled as likely-"phenotype" and were visually reviewed before being reassigned into the right phenotype group. If a cell could not be confidently categorized into any phenotype, it was labelled as “Unknown”, “Myeloid” or “Lymphoid” and later removed from downstream analyses. NK cells were also excluded due to low cell counts and absence of the NKG2a marker expression in part of the samples.

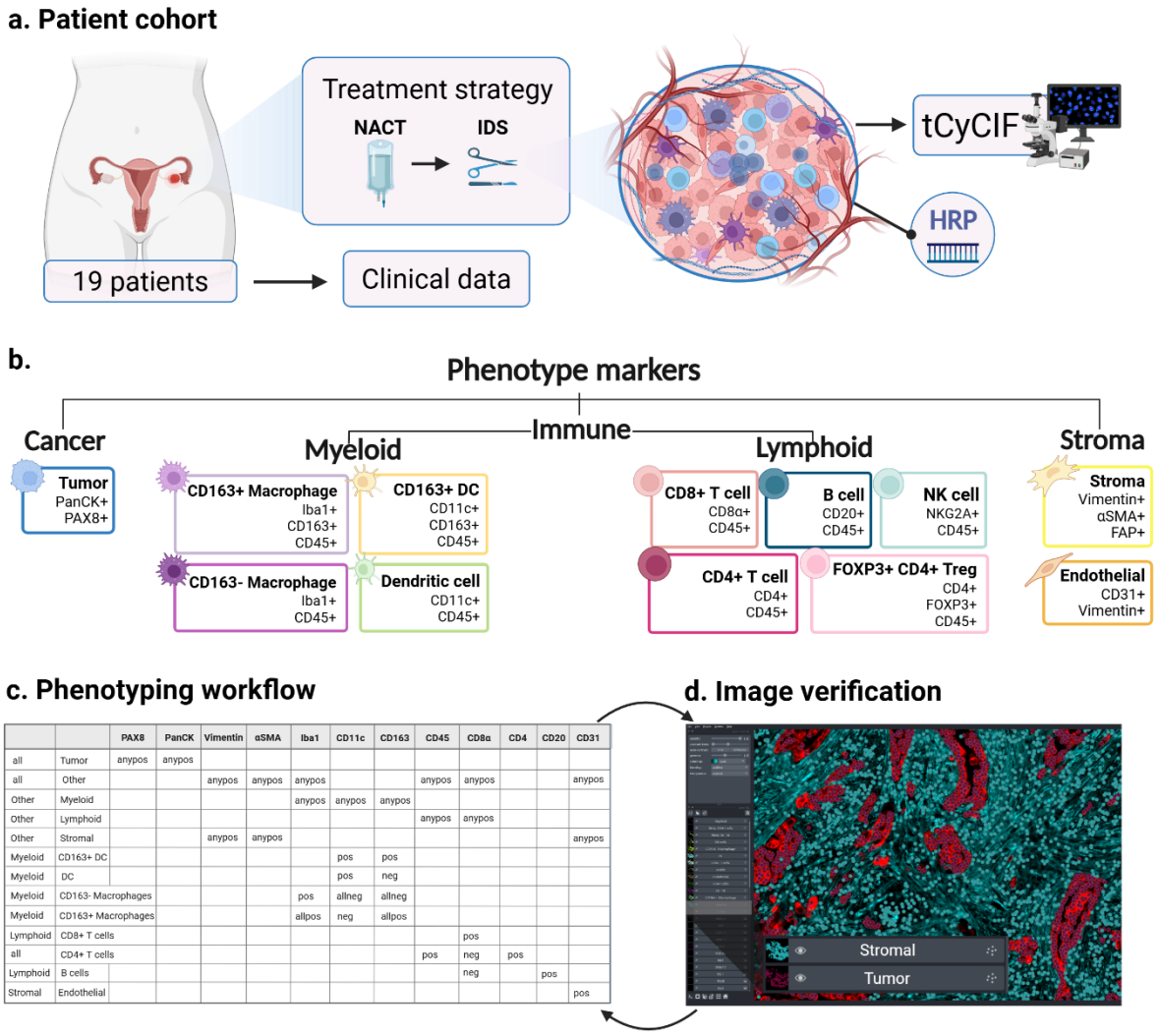

		PAX8	PanCK	Vimentin	αSMA	Iba1	CD11c	CD163	CD45	CD8α	CD4	CD20	CD31
all	Tumor	anypos	anypos										
all	Other			anypos	anypos	anypos			anypos	anypos			anypos
Other	Myeloid					anypos	anypos	anypos					
Other	Lymphoid								anypos	anypos			
Other	Stromal			anypos	anypos								anypos
Myeloid	CD163+ DC						pos	pos					
Myeloid	DC						pos	neg					
Myeloid	CD163- Macrophages					pos	allneg	allneg					
Myeloid	CD163+ Macrophages					allpos	neg	allpos					
Lymphoid	CD8+ T cells									pos			
all	CD4+ T cells								pos	neg	pos		
Lymphoid	B cells									neg		pos	
Stromal	Endothelial												pos

Figure 1. Overview of the cohort and phenotyping process. **a.** The cohort consists of 19 HR-proficient HGSC patients, treated with NACT and IDS. Clinical data, including PFS, were used to divide patients into short, intermediate and long PFS groups. Tumor samples, obtained as FFPE blocks, were imaged using tCycIF imaging, and HR testing was performed. **b.** 15 phenotype markers were used to classify 12 distinct phenotypes. **c.** The phenotyping process involves constructing a sample-specific logic table to define which markers each phenotype is positive for. **d.** Image verification was performed in Napari, using phenotype masks on tCycIF images to ensure accurate phenotyping. Figure created with Biorender.com.

3.2.3 Single-cell spatial analysis

Spatial analyses were performed using Scimap in Python within Jupyter Notebook (Nirmal & Sorger, 2024). RCNs were identified using two approaches: spatial count and Latent Dirichlet Allocation (LDA).

Spatial count was computed using the tl.spatial_count function, which quantifies the proportion of neighboring cells for each cell-of-origin within a specified radius. The

radius was measured from the center of each cell, including all neighboring cells whose centers fell within the defined radius. Three radii were computed: 13 microns, 25 microns and 35 microns.

For LDA, the tl.spatial_lda function was used to construct a neighborhood matrix for each cell, incorporating all neighboring cells within the defined radius. LDA then identifies spatial motifs based on phenotype co-occurrence patterns. The model was computed with three radii (13, 25 and 35 microns) and a total of 10 latent motifs, corresponding to the number of phenotypes used in neighborhood calculations.

Both spatial count and LDA results were clustered using K-means clustering via the tl.spatial_cluster function. The optimal number of clusters (k) for each radius was determined using the elbow method, identified with the KneeLocator function from the kneed Python package (Arvai, 2020). This method finds the “elbow” point of a curve, which is defined as the point with the maximum curvature, where the rate of change in the data decreases most sharply. The optimal k value from the KneeLocator was then visualized using the KElbowVisualizer from the YellowBrick Python package to plot the elbow curve (Bengfort & Bilbro, 2017).

Each cluster from both methods was characterized based on the proportion of phenotypes within it. Cluster identities were determined using bar plots generated with pl.stacked_barplot, alongside visualizations of clusters overlaid on tCyCIF images using the pl.image_viewer function.

The RCNs were annotated based on their cellular composition and proximity to tumor cells. Tumor RCNs were annotated as tumor core when they consisted solely of tumor cells and were not infiltrated by other cell types. Stromal RCNs were classified into two categories: immune infiltrated stromal RCNs, which contained immune cells close to stromal cells, and immune excluded stromal RCNs, which consisted only of stromal cells without immune infiltration. In cases where stromal RCNs could not be clearly classified, they were labeled as Stroma 1, Stroma 2, and so on. Tumor-stroma interface (TSI) RCNs were annotated as TSI, followed by the most abundant cell type, such as TSI - stroma. In instances where the differences between TSI RCNs were not distinguishable, they were further labeled as TSI 1 and TSI 2. Immune RCNs were annotated based on the most abundant immune cell type present within the RCN. In

cases where a mix of several immune cell types was present in similar proportions, these RCNs were labeled as Immune compartment.

3.2.4 Statistical analysis and visualization in R

Analyses were performed using R version 4.4.0. The distribution of global and immune cell types across patients was visualized using ComplexHeatmap (v2.20.0) and ggplot2 (v3.5.1). Hierarchical clustering was performed using Ward's method with Euclidean distance. Z-score normalized heatmaps were generated with ComplexHeatmap, with PFS included as row annotations for all heatmaps. To visualize the distribution of cell types and immune infiltration across patients, bar plots and box plots were created using ggplot2. Additionally, dot plots were generated to display the $\log_2$ fold change in the proportions of clusters between the "Long" and "Short" PFS groups across different radii.

For Clustree analysis, hierarchical relationships between clusters across spatial radius scales (13 µm → 25 µm → 35 µm) were visualized using clustree (v0.4.0), with transitions below 10% of the RCN excluded.

To assess the diversity of phenotypes within clusters, Shannon's Entropy Index and Simpson's Diversity Index were calculated using the vegan package (v2.6-2). Wilcoxon rank-sum tests were performed to compare immune cell abundances between RCNs and clinical groups across different RCNs.

3.2.5 Code availability

All code used in this thesis is available on GitHub at:
https://github.com/alvagronholm/Masters-thesis

4 Results

4.1 Multiplexed imaging enables detailed characterization of the TME at a single-cell level

A total of 19 HRP patient samples were analyzed, all of which were obtained from interval debulking surgeries performed on patients who had previously undergone platinum-based chemotherapy. The median PFS of the cohort was 14.2 months. Based on PFS, the cohort was divided into three groups: 6 patients in the short PFS group, 6 patients in the intermediate PFS group, and 7 patients in the long PFS group.

4.1.1 tCycIF analysis reveals spatially resolved phenotypes in the TME

To obtain a detailed single-cell characterization of the spatial TME, tCycIF imaging was performed across all samples, targeting 36 different proteins. Cell type annotations were based on 14 phenotype markers (Fig. 2a). In total, 6,470,187 single cells were identified and phenotyped across the 19 samples based on their marker expression profiles, using Scimap (Methods) (Nirmal & Sorger, 2024).

Out of the 6,470,187 phenotyped single cells, 2,975,491 (46%) were classified as tumor cells, 1,768,792 (27%) as stromal and endothelial cells, and 1,725,904 (27%) as immune cells.

Across the full cohort, stromal cells comprised 24% of all cells, with CD31+ endothelial cells representing 2.9%. Among myeloid cells, CD163+ macrophages made up 2.9%, CD163- macrophages 3.6%, CD163+ DCs 5.9%, and DCs 6.8%. Lymphocyte populations included 3.9% CD8+ T cells, 2.1% CD4+ T cells, 0.5% FOXP3+ CD4+ Tregs, and 1.0% B cells. Cells that could not be confidently assigned a phenotype were removed from further analysis, resulting in the exclusion of a total of 48,478 cells (0.75%).

The accuracy of phenotyping was extensively validated through visual confirmation, overlaying cell annotation masks onto tCycIF images using a customized Napari plugin (Methods) (Sofroniew et al., 2025). Multiple phenotype markers were visualized simultaneously, revealing distinct and spatially separable expression patterns that support accurate cell type identification (Fig. 2b). The assigned phenotypes were consistent with the expected marker expression profiles (Fig. 2c). Tumor cells, the most

abundant phenotype, exhibited strong PanCK expression, while stromal and endothelial cells were marked by Vimentin, αSMA, and CD31, respectively. Immune subsets displayed distinct marker profiles, including CD8a for CD8+ T cells and IBA1 for macrophages.

In conclusion, phenotyping allowed for an accurate and spatially resolved identification of multiple cell types. The associated labels are concordant with the expected morphology and marker expression profiles, as shown in Fig. 2.

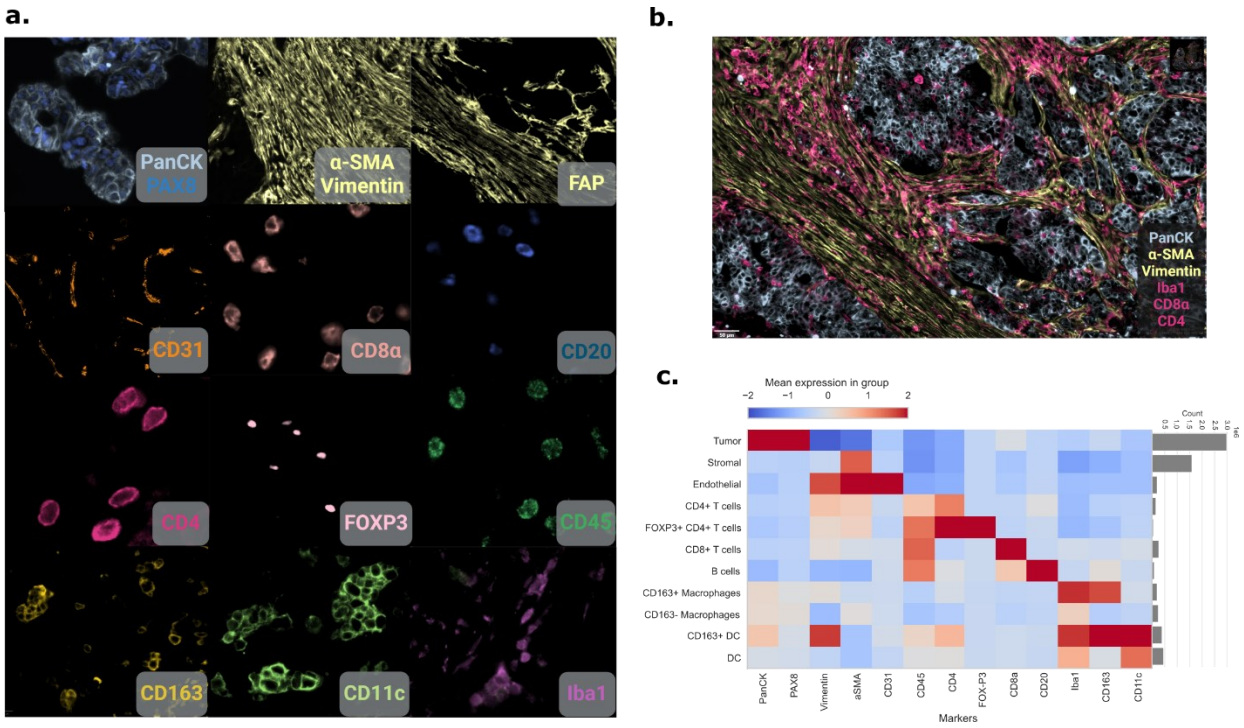

Figure 2. a. Marker panel used for phenotyping, illustrating clear and specific expression patterns. **b.** Representative tCycIF image showing simultaneous visualization of multiple markers with spatially distinct expression patterns. **c.** Heatmap showing distinct marker expression profiles for each cell type, confirming accurate phenotypic characterization, with tumor cells identified as the most abundant population. Figures a and b were created with Biorender.com

4.1.2 Composition analysis highlights unique TME profiles across patients

Next, we evaluated the proportions of different cell types within the TME across the patient cohort to explore the diversity of phenotype composition.

As expected, the composition of global cell types, tumor, stromal and immune, was unique for each patient (Fig. 3a). Hierarchical clustering of the relative proportions of the global cell types identified two distinct patient clusters. The first cluster, annotated with a green box, exhibited a lower abundance of tumor cells and a higher abundance

of stromal cells, while the second cluster, annotated with an orange box, was characterized by a higher proportion of tumor cells and a lower proportion of stromal cells. Immune cell proportions varied both within the clusters and within patient groups. Interestingly, the cluster with a higher proportion of stromal cells (green box) only included patients from the short and intermediate PFS groups, while the cluster with a higher tumor proportion (orange box) contained patients from all PFS groups.

Similarly, the composition of the tumor immune microenvironment (TIME) was patient-specific and varied considerably across patients, with DCs being the most abundant immune cell type (Fig. 3b). Hierarchical clustering of the relative proportions of immune cells revealed several different patient clusters, further highlighting the heterogeneity of the immune landscape within the TME. Notably, one cluster, annotated with a red box, was characterized by a high abundance of CD8+ T cells, with most patients in this group belonging to the short PFS group and one patient from the intermediate PFS group.

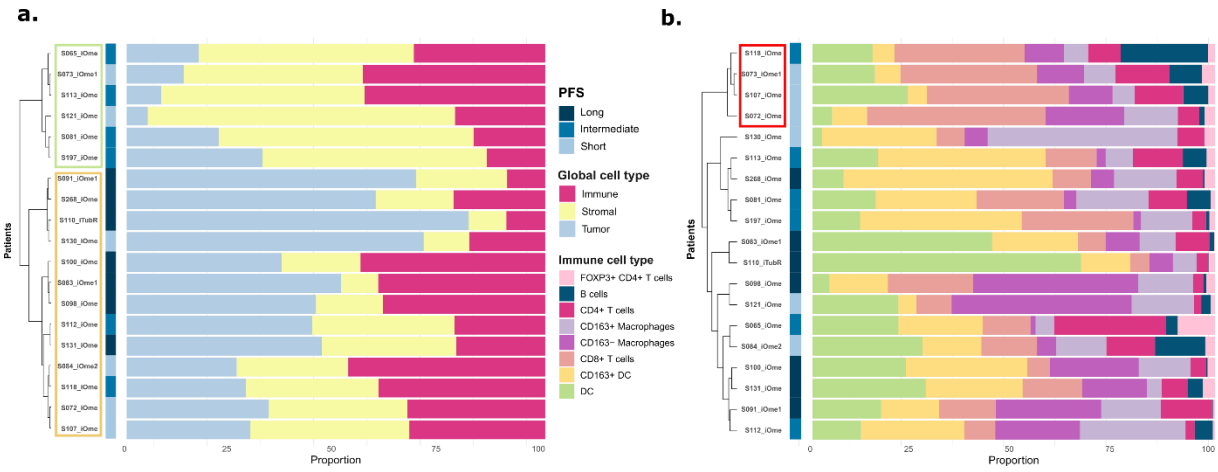

Figure 3. a. Annotated barplot of global cell types (tumor, stromal, and immune) ordered by hierarchical clustering. Cluster 1 (green) is characterized by a higher stromal composition, while cluster 2 (orange) has a higher tumor composition. PFS annotations are shown for each patient in both figures: patients below the 33rd percentile labeled as “short”, those above the 66th percentile as “long”, and those in between as “intermediate”. **b.** Annotated barplot depicting immune subtype composition across the cohort, ordered by hierarchical clustering, revealing distinct TIME profiles. The cluster marked in red shows a high abundance of CD8+ T cells relative to other clusters.

4.2 Comparison of spatial count and LDA reveals method- and radius-dependent changes in the composition and diversity of RCNs

Understanding the spatial organization of cells in the TME has the potential to reveal novel insights into the tumor architecture, disease progression and therapeutic responses. The spatial patterns of different phenotypes within the TME are intrinsically linked to biological processes, such as immune evasion, angiogenesis, and metastasis. By characterizing the arrangement of these specific cellular neighborhoods, spatial analysis can offer important insights into tumor heterogeneity and potential factors that may influence therapeutic outcomes.

Here, we employed two computational approaches, spatial count and LDA, to analyze the spatial organization of cellular distributions at multiple scales. These methods were applied using predefined radii of 13, 25, and 35 microns to capture cellular interactions as well as larger regions across different distances, thereby allowing us to identify biologically relevant spatial patterns.

Spatial count uses a predefined radius approach to identify RCNs in the TME (Fig. 4a). In contrast, LDA employs a probabilistic modeling method to uncover latent spatial motifs based on the neighborhood matrix, ultimately defining RCNs (Fig. 4b). By applying both spatial count and LDA, we can assess how these methods differ in capturing the spatial architecture of the TME. Spatial count provides a more discrete classification of cellular neighborhoods, whereas LDA allows for a probabilistic, gradient-like assignment of spatial motifs. Comparing the results from both approaches enables us to determine which method is more suitable for different types of spatial analyses. Additionally, by analyzing multiple radii, we can evaluate how neighborhood size influences the detection of spatial patterns and whether certain biological insights are more prominent at specific scales.

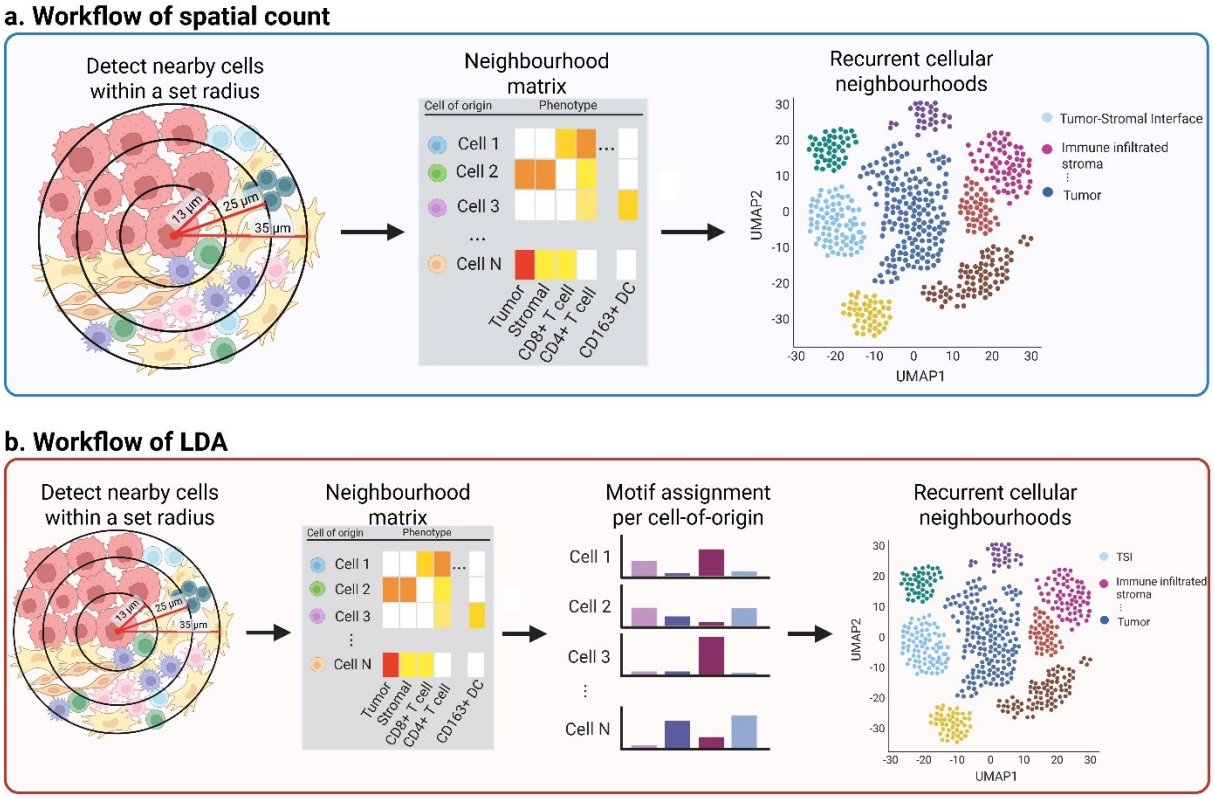

Figure 4. Workflow schematic of spatial count and LDA for defining RCNs. **a.** Spatial count computes a neighborhood matrix based on a predefined radius. Here, radii of 13, 25, and 35 microns were used. Clustering of the neighborhood matrix identified RCNs. **b**. LDA generates a neighborhood matrix based on a predefined radius (here 13, 25, and 35 microns) and applies probabilistic modeling to uncover spatial motifs. Clustering of these motifs identifies the RCNs. Figure created using Biorender.com.

4.2.1 Cell-type size variation influences neighbor identification across spatial scales

To better understand how the choice of radius impacts spatial analysis, it is important to consider the physical scales of different cell types. Cell size directly influences how many neighboring cells are captured within a given radius, as larger cells occupy more space, potentially limiting the number of surrounding cells included in a spatial neighborhood. Additionally, the spatial distribution of different cell types, whether they exist in dense clusters or more dispersed patterns, further affects the number of neighboring cells identified.

To illustrate these variations, representative measurements from a tCycIF image highlight differences in cell morphology (Fig. 5a). Cell measurements obtained from the images indicated approximate radii of 12 µm for tumor cells, 6 µm for stromal cells, 10 µm for macrophages, 5 µm for CD4+ T cells, and 4 µm for CD8+ T cells, with considerable variation in eccentricity. These cell size differences play a crucial role in

the selection of the spatial radius for analysis. The chosen radii (13, 25, and 35 μm) were designed to capture different spatial scales within the TME. At the smallest radius (13 μm), only immediate neighboring cells are typically included, and direct neighbors for larger cells may be excluded. In contrast, the largest radius (35 μm) captures a broader range of neighboring cells, extending beyond immediate cell-cell interactions.

To quantify how these differences impact spatial organization, we assessed the median number of neighboring cells for different phenotypes (Fig. 5b). As expected, tumor cells, which are typically densely clustered, consistently exhibited the highest number of neighboring cells, with values increasing as the radius expanded. In contrast, stromal cells, being large and more dispersed, had fewer neighbors across all radii. Macrophages, which often reside together and at tumor-stroma interfaces, showed intermediate values, while T cells, despite their smaller size, had relatively few neighbors due to their more scattered distribution within the stroma. These patterns highlight how both cell size and spatial arrangement influence the number of neighboring cells detected at different scales.

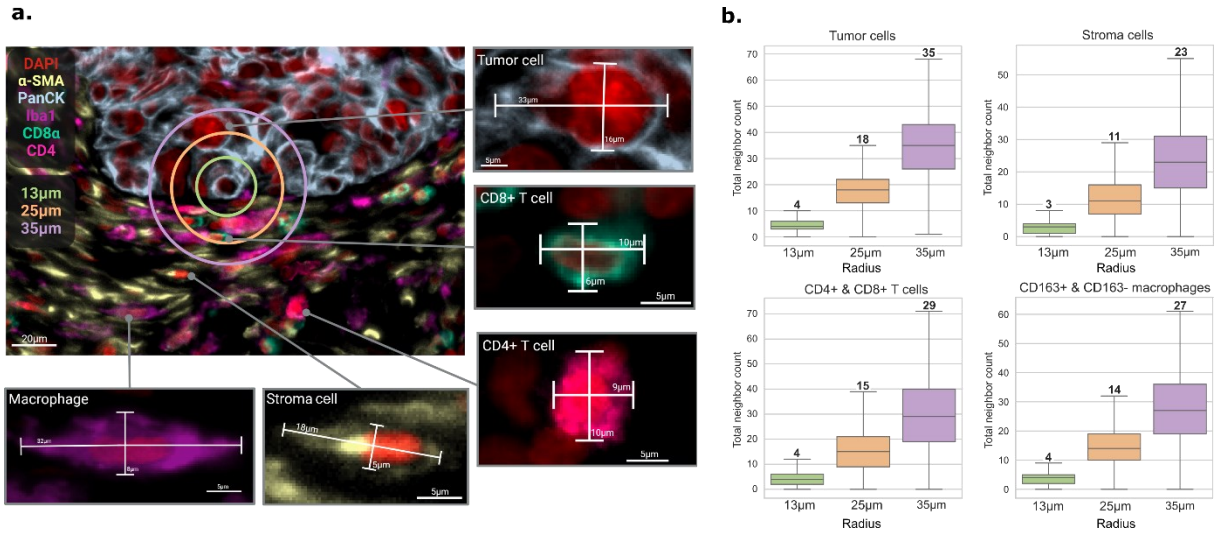

Figure 5. a. Representative tCycIF image illustrating the spatial area covered by each radius (13, 25, and 35 microns) from a single cell-of-origin, with example cell size measurements shown for different cell types. **b.** Cell-type specific boxplots showing the distribution of neighboring cell counts across radii of 13, 25, and 35 microns. Median values are indicated above each box. Figure a was created using Biorender.com.

4.2.2 Spatial count and LDA detect distinct scale-dependent spatial patterns in tumor, stromal, and immune microenvironments

A total of 6,470,187 single cells were clustered based on their neighborhood characteristics computed with spatial count and LDA (Methods). Clustering revealed 12-15 distinct RCNs for each radius, as determined by the elbow plots (Supplementary Figure 1). Despite variation in clustering details, four major RCN types were consistently observed across methods and radii: (1) Tumor RCNs, (2) Stromal RCNs, (3) TSI RCNs, with mixed stromal and immune cells close to tumor cells and (4) Immune cell RCNs. While these RCN classes were broadly consistent, their specific cellular compositions varied significantly by method and radius.

Spatial count captures scale-dependent shifts in cellular composition

In the spatial count method, the composition of RCNs changes noticeably with increasing spatial radius (Fig. 6a). The tumor core RCN, predominantly composed of tumor cells, remains distinct across all radii and both methods. At small radii, clustering reflects highly localized tumor microenvironments with minimal inclusion of non-tumor cells. As the radius increases, tumor cells become associated with more diverse neighbors, shifting into TSI RCNs, reflecting the breakdown of strict tumor boundaries and increasing interaction with the surrounding microenvironment.

Within the stromal and immune compartment, at small radii (13 μm), RCNs are dominated by close, cell-type-specific interactions, such as endothelial-endothelial or DC-DC interactions. As the radius increases to 25 μm and 35 μm, these RCNs begin to incorporate larger tissue structures. For instance, the endothelial RCN includes not only endothelial cells but also surrounding stromal and immune cells, resulting in more heterogeneous and integrated cellular environments (Fig 6b). This scale-dependent compositional shift is supported by diversity indices, which show an increase in heterogeneity, especially between 13 μm and 25 μm for endothelial cells and DCs (Fig. 6c). Interestingly, compared to spatial count, LDA is more homogenous at smaller radii but shows a more pronounced increase in heterogeneity as the radius increases. The increase in heterogeneity highlights the transition from localized microenvironments to broader, multicellular tissue contexts at larger scales.

Furthermore, across all radii, spatial count excelled at detecting spatially restricted structures, such as blood vessels and TLSs, which consist of similar cell types, resulting in similar spatial neighborhoods.

In contrast, CD4+ T cells and macrophages, which are more diffusely distributed within the TME, are primarily detected at small radii, where clustering is mainly based on direct cell-to-cell interactions and only a few neighboring cells. As the radius expands, these cells become integrated into larger immune environments, dissolving their distinct neighborhoods into broader immune RCNs, such as the "immune compartment" RCN. Thus, spatial count remains scale-dependent, capturing specific spatial interactions at smaller radii while integrating broader tissue structures at larger ones.

LDA maintains spatial coherence across radii

In contrast, LDA maintains stable and coherent spatial patterns across all radii, preserving the organization of spatial landscapes even at smaller scales and retaining spatial context as the radius increases (Fig. 6a).

Immune cell RCNs in particular preserve their distinct organization, rather than integrating into broader compartments. For example, at 13 μm, CD163+ macrophages form two distinct RCNs: one associated with stromal interactions and another composed of mixed CD163+ and CD163− macrophages with B cells. As the radius increases, one macrophage-associated RCN remain distinct, highlighting LDA's ability to retain localized spatial features. Similarly, CD4+ T cells consistently form distinct RCNs at all radii. At 13 μm, LDA can even distinguish between a stromal-associated CD4+ RCN and a CD4+ dominant RCN, capturing fine-grained spatial differences not apparent in spatial count.

B cells, however, exhibit contrasting clustering behaviors between scales, as their spatial context evolves. B cells are often found in TLSs in the TME, surrounded by aggregations of immune cells, such as DCs and macrophages. (I) At 13 μm, they are found in proximity to macrophages, indicating localized immune interactions. (II) At 25 μm, they cluster predominantly with other B cells, emphasizing their self-aggregating nature. (III) By 35 μm, B cells integrate into a broader immune landscape, clustering with CD163+ DCs. This scale-dependent clustering behavior in LDA reflects shifts in the local spatial context of B cells.

Spatial count reveals greater RCN diversity, while LDA results in more homogeneous neighborhoods

Comparison of spatial count and LDA showed that LDA RCNs are generally more homogeneous, particularly at smaller radii. Diversity index comparisons revealed that spatial count exhibited higher values across all radii for the “Tumor core” RCN (Fig. 6d). For the “Stroma, immune excluded” RCN at the smallest radii, spatial count also displayed significantly higher diversity than LDA. Additionally, LDA captured significantly fewer immune cells compared to spatial count across samples at 13 μm ($p = 6.6e-7$) (Fig. 6e).

Furthermore, these findings suggest that spatial count is more confined to scale-dependent interactions, with its results reflecting the immediate cellular environment at smaller radii and incorporating broader features at larger radii. In contrast, LDA is more robust to noise, identifying spatial landscapes even at smaller scales and maintaining stable localized immune structures. As the radius increases, LDA continues to preserve these patterns better, whereas spatial count integrates broader tissue structures, leading to a more heterogeneous composition at larger radii.

a.

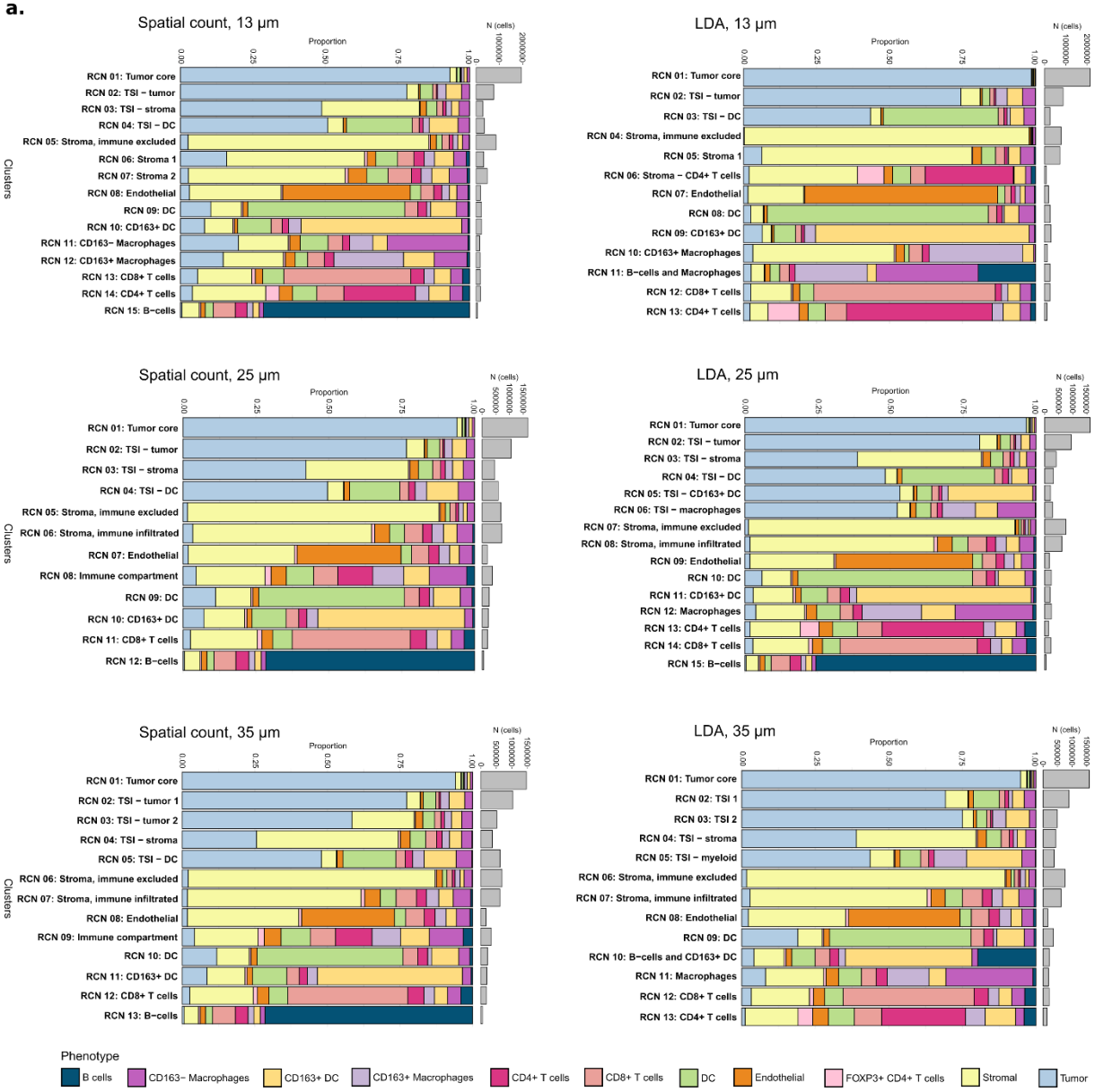

Figure continued on next page.

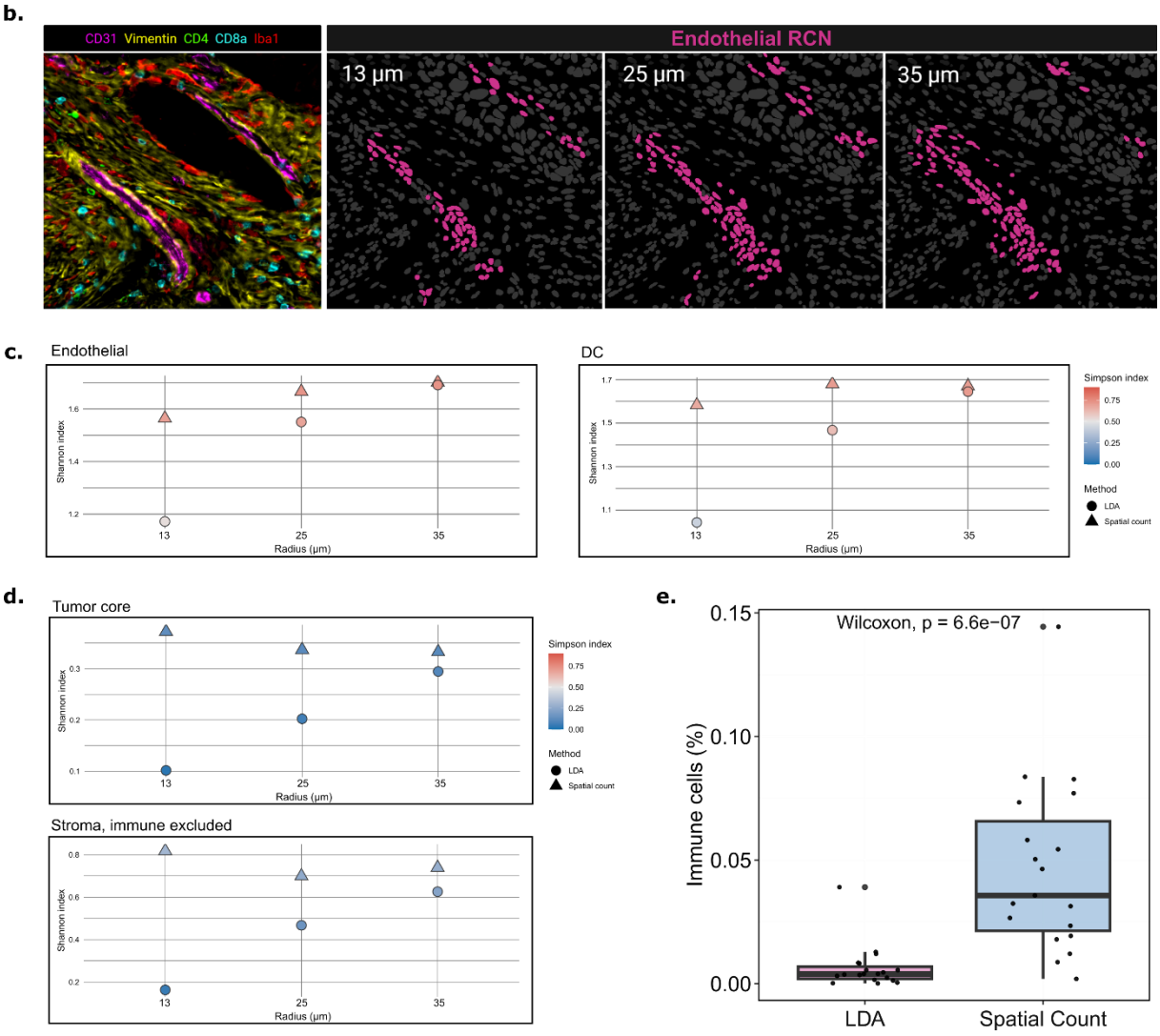

Figure 6. a. Barplots showing the composition of phenotypes within each RCN across spatial count and LDA at spatial radii of 13 µm, 25 µm, and 35 µm. The cell count in each RCN is shown in grey. **b.** Left panel shows a tCycIF snapshot with phenotype markers. The subsequent panels show the endothelial RCN at 13 µm, 25 µm, and 35 µm radii in spatial count, illustrating how the RCN composition becomes more diverse as the radius increases. **c.** Shannon and Simpson's diversity indices for "Endothelial" and "DC" RCNs, plotted across all radii and both methods. **d.** Shannon and Simpson's diversity indices for "Tumor core" and "Stroma, immune excluded" RCNs, plotted across all radii and both methods. **e.** Boxplot showing the percentage of immune cells in the "Stroma, immune excluded" RCN at 13 µm for LDA and spatial count. Individual points represent immune cell percentages for each sample. Statistical significance was determined using the Wilcoxon test.

4.2.3 Tracking changes in cellular neighborhoods across spatial scales reveals grouping, splitting, and reorganization of cells

We next analyzed how RCNs evolve across different spatial scales using clustree analysis, which provides valuable insights into the hierarchical relationships between

RCNs. This approach highlights patterns of merging, splitting, and reorganization, allowing us to track how cellular neighborhoods change as the spatial radius expands. While some RCNs remain stable across radii, others undergo substantial restructuring, reflecting variations in how different spatial scales capture cellular interactions.

Most changes in RCN composition occur between 13 µm and 25 µm

In the spatial count method, most observed shifts occur between the 13 µm and 25 µm radii. The largest splits are observed in the "Tumor core", "TSI-tumor" and stroma RCNs, reflecting the increasing diversity of neighboring cells at larger scales (Fig. 7a). Additionally, at 25 µm, a distinct "immune compartment" RCN emerges, composed of various immune cells from previously separate immune RCNs, including CD4+ T cells and CD163- macrophages, as well as cells from the stroma RCNs with immune infiltration ("Stroma 1" and "Stroma 2"). Increasing the radius from 25 µm to 35 µm results in fewer changes, with immune cell RCNs remaining consistent.

In LDA, a more pronounced splitting pattern is observed between radii, with most divergence seen between 13 and 25 µm (Fig. 7b). The majority of splits are concentrated within the tumor core and the RCNs near the tumor, with cells at the tumor border becoming more distinct and forming separate RCNs. In contrast, immune cell RCNs remain relatively consistent across radii, with the CD4+ T cell RCN staying distinct and uniform across all scales. However, as noted previously, B cells exhibit variability in LDA, clustering with macrophages at 13 µm and with CD163+ DCs at 35 µm, highlighting shifts in spatial associations among some immune cells across scales.

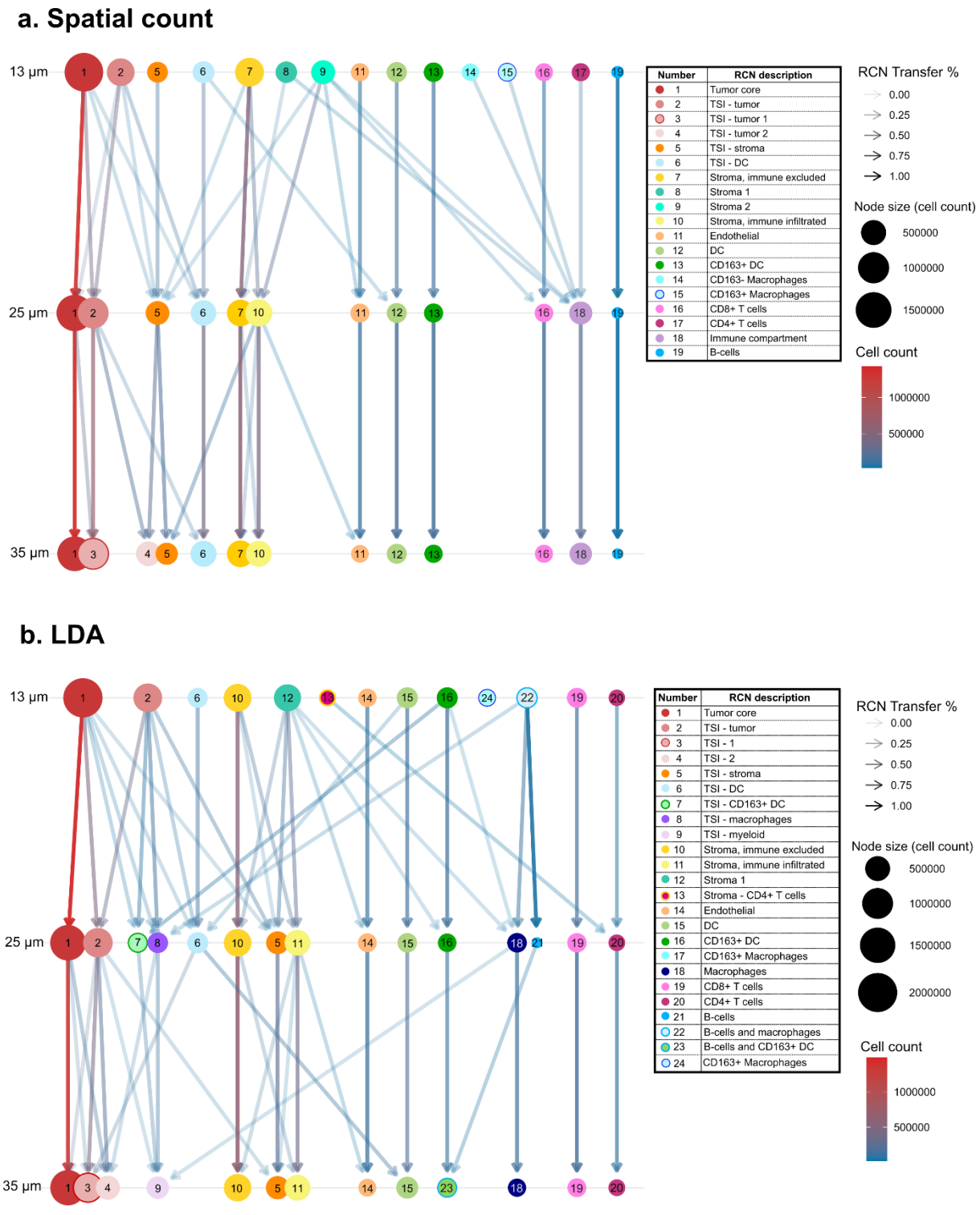

Figure 7. Clustree diagrams showing the hierarchical relationships between RCNs across spatial scales (13 µm → 25 µm → 35 µm) using **a.** spatial count and **b.** LDA. The diagrams illustrate how clusters evolve as the spatial radius increases, with node size representing the number of cells within each RCN. Edge color shows the cell count that has transitioned into a particular RCN, and edge color intensity indicates the percentage of cells that have moved into a specific RCN. Edges representing fewer than 10% of the total population have been excluded.

Spatial count shows RCN convergence with increasing radius, while LDA tends to maintain distinct RCNs

A key distinction between the two methods is how they diverge across spatial scales. LDA, particularly at the 13 μm radius, demonstrates a greater tendency to split some RCNs into finer subclusters, while preserving certain cell type-specific RCNs, highlighting its ability to better distinguish between cell types. In contrast, the spatial count method tends to converge, with RCNs merging into broader categories across radii. For instance, immune RCNs such as CD4+ T cells, CD163+ macrophages, and CD163- macrophages merge into a broader immune compartment as the radius increases. In LDA, these immune cell types remain more distinct across all radii, reflecting its greater tendency for divergence and finer differentiation of cell types.

The tumor core RCN is the largest RCN across all radii and both methods. As the radius increases to 25 μm, the tumor core RCN diverges into several distinct RCNs, including TSI-tumor and TSI-stroma. At 13 μm, the tumor core splits into six RCNs in LDA and four in spatial count, whereas at 25 μm, it splits into three in LDA and two in spatial count. TSI RCNs are more diffuse at smaller radii, encompassing a wider variety of neighboring cell types. As the radius increases, TSI RCNs become more structured and distinct, with the clustree analysis showing a clear reorganization into new subtypes between 13 and 25 μm. By 35 μm, the TSI-tumor RCN splits further into two separate RCNs, contributing to a more organized architecture around the tumor. Interestingly, the TSI RCNs appear more distinct in spatial count than in LDA (Fig. 8).

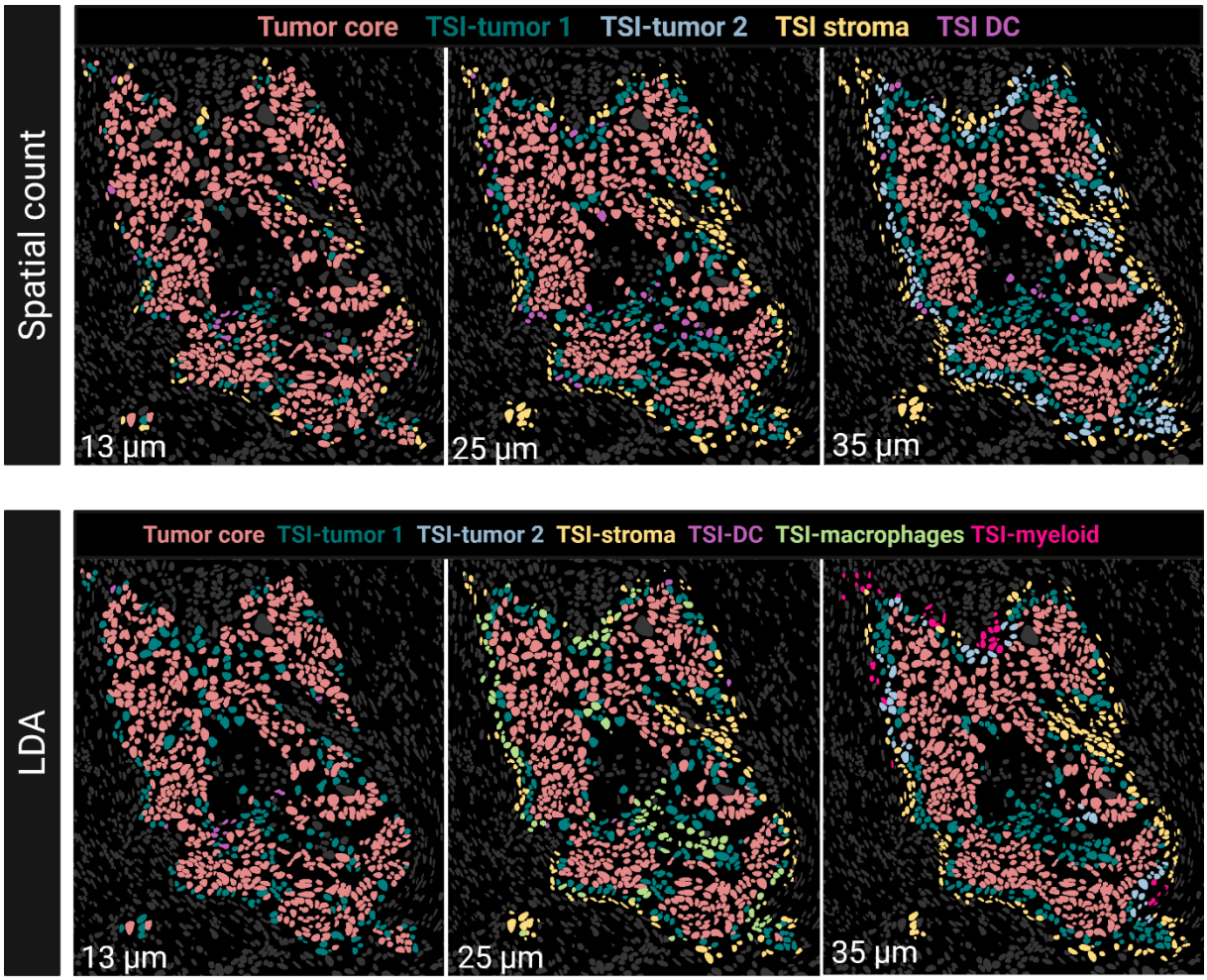

Figure 8. Representative RCN masks computed using spatial count (top) and LDA (bottom) at 13 µm, 25 µm, and 35 µm radii. As the radius increases, the tumor core RCN splits into more distinct TSI RCNs. Spatial count shows more spatially defined TSI RCNs, especially at larger radii, while LDA identifies a broader variety of TSI RCNs overall.

As shown previously, endothelial RCNs increase in heterogeneity as the spatial scale expands, primarily due to the broader neighborhood of cells captured around the blood vessels. In both methods, the clustree analysis reveals that the endothelial RCN identified at smaller radii is preserved as the radius increases, but it becomes increasingly integrated with surrounding cells from stroma RCNs that contain immune infiltration. This transition reflects the growing complexity of the cellular environment as larger regions of the tissue are captured, with the endothelial RCNs blending into more heterogeneous structures that incorporate immune cells and stromal components.

4.2.4 Spatial distribution and enrichment of RCNs across clinical groups show consistent trends across methods and radii

Next, we analyzed the distribution of RCNs across distinct clinical groups to determine whether spatial neighborhood composition is associated with clinical outcomes. By comparing patients in the short and long PFS groups, we examined how spatial scale and computational methods influence the detection of clinically relevant differences.

Hierarchical clustering of the relative abundances of RCNs revealed similar patient clustering across both methods and radii, with a clear distinction between clinical groups (Supplementary Figure 2).

In the spatial count method, enrichment patterns of specific RCNs in the short and long PFS groups remained consistent across all radii (Fig. 9a). RCNs for “Stroma, immune excluded”, “Endothelial”, and “CD8+ T cells” showed increasing enrichment in the short PFS group as the radius increased. The observed enrichment of CD8+ T cells in the short PFS group aligns with the earlier findings from the composition analysis of immune cells. Additionally, immune-infiltrated stromal RCNs (“Stroma, immune infiltrated”, “Stroma 1” and “Stroma 2”) were enriched in the short PFS group, while “tumor core” and “TSI-tumor” RCNs were consistently enriched in the long PFS group.

The LDA method produced similar enrichment trends across clinical groups (Fig. 9b). Again, stromal RCNs were enriched in the short PFS group, while “tumor core” and “TSI-tumor” RCNs were more abundant in the long PFS group. However, B cell-associated RCNs displayed more variability. At 13 μm, B cells clustered with macrophages, while at 35 μm, they clustered with CD163+ DCs, leading to different enrichment trends. B cell RCNs were generally enriched in the short PFS group. However, when associated with CD163+ DCs, they showed enrichment in the long PFS group, while B cells clustered with macrophages showed lower enrichment in the short PFS group.

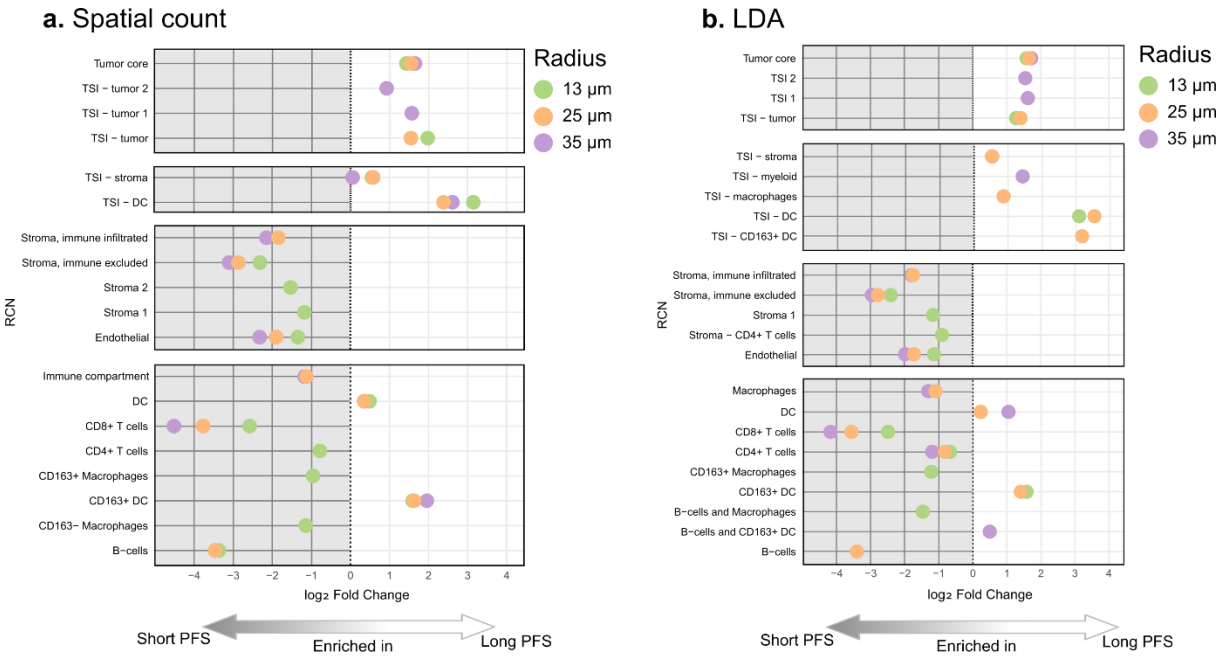

Figure 9. a. Dotplot showing $\log_2$ fold change in RCN enrichment between short and long PFS groups at 13 µm, 25 µm, and 35 µm radii using spatial count. Positive values indicate enrichment in the long PFS group, while negative values indicate enrichment in the short PFS group. **b.** Dotplot showing the same analysis as (a) but using LDA. Similar to (a), positive values indicate enrichment in the long PFS group, while negative values indicate enrichment in the short PFS group.

Overall, both methods and radii captured similar trends in RCN enrichment across clinical groups, with the largest radius showing the most extreme enrichment in most RCNs. Endothelial cells showed consistent enrichment in the short PFS group ($p<0.05$) (Fig. 10). Furthermore, stromal RCNs were consistently enriched in the short PFS group, reflecting the higher abundance of stromal cells observed in the global cell type composition analysis. The spatial analysis further differentiated the stroma into immune-excluded and immune-infiltrated regions, revealing that immune-infiltrated stroma was significantly associated with the short PFS group across radii and methods ($p<0.05$). In contrast, immune-excluded stroma showed a weaker enrichment trend in the short PFS group.

The tumor core showed a modest increase in enrichment across methods and radii in the long PFS group, while TSI-tumor RCNs, located at the tumor border, displayed a stronger enrichment trend in the long PFS group. At the largest radius, TSI-tumor further divided into two RCNs, with the one in closer proximity to the tumor core (TSI-tumor 1 and TSI-1) showing a more pronounced enrichment in the long PFS group. This trend was more pronounced in LDA ($p=0.0082$) compared to spatial count ($p=0.051$).

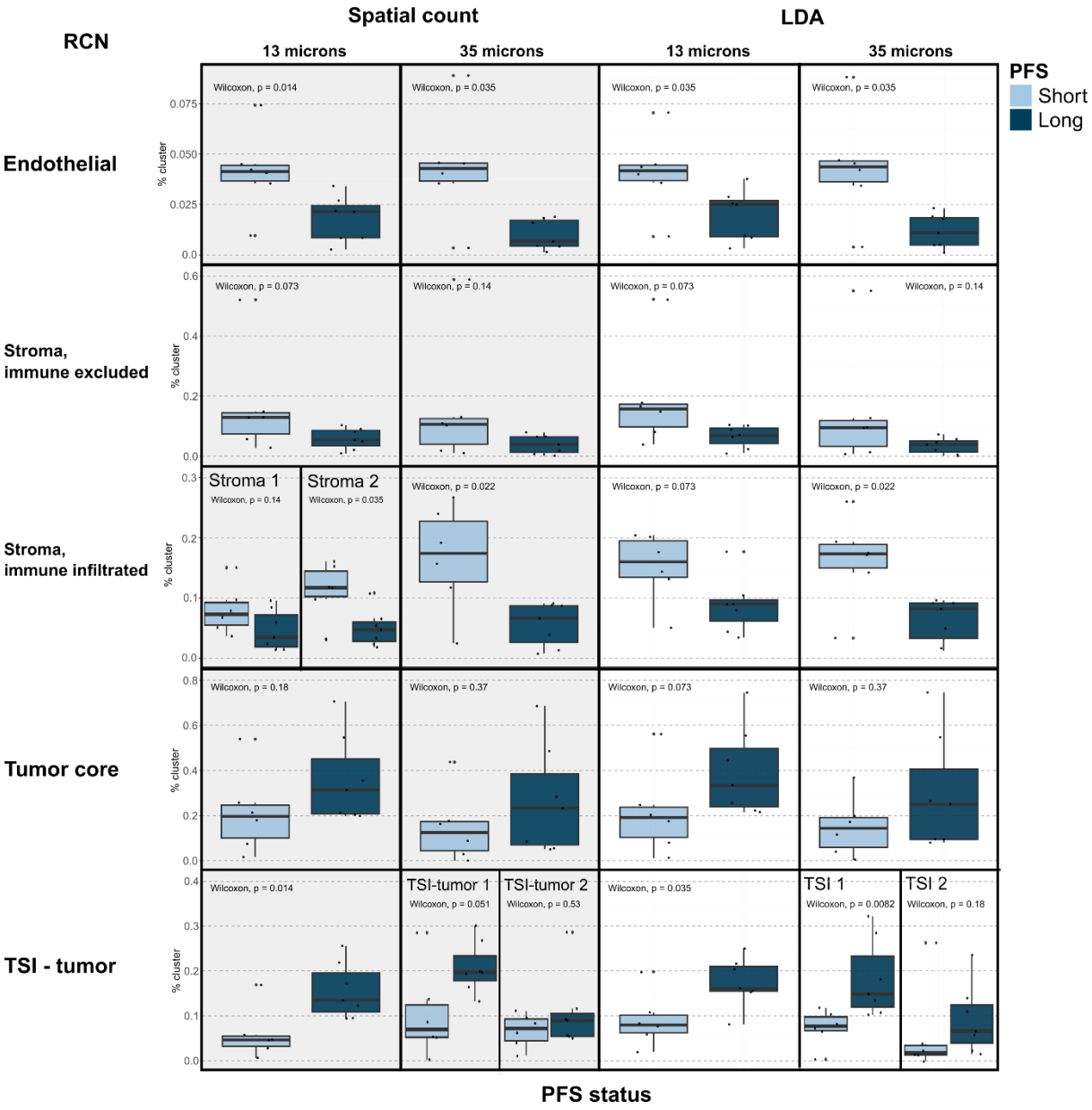

Figure 10. Comparison of RCN enrichment across radii and methods. For clarity, we focus on comparing the smallest (13 μm) and the largest (35 μm) radii. Boxplots show the percentage abundance of each RCN in short (light blue) and long (dark blue) PFS groups across five RCNs. For some spatial scales, two similar annotated RCNs exist, both of which are included here. Wilcoxon p-values are shown for each boxplot, indicating statistical significance of enrichment differences between clinical groups.

5 Discussion

Studying the TME is crucial for understanding the complexity of disease progression and therapeutic resistance in HGSC (Rodriguez et al., 2018). In particular, analyzing the spatial organization within the TME can reveal clinically relevant features, such as differences among patient subtypes (Launonen et al., 2022), treatment-induced changes (Liu et al., 2021), or patient prognosis (Nirmal et al., 2022). Advances in highly multiplexed imaging, coupled with computational approaches, now allow for the detection of fine-grained spatial patterns that are often invisible to the human eye (T. Fu et al., 2021; Lin et al., 2018). However, the most suitable approach for analyzing the spatial architecture of the TME remains unclear.

In this study, we aimed to evaluate and compare two such methods, spatial count and LDA, for their ability to identify relevant spatial structures across different spatial scales. By phenotyping 6.47 million single cells, we identified distinct tumor, stromal, and immune subtypes, revealing interpatient heterogeneity in both global cell composition and immune microenvironments. These findings highlight the complexity of HGSC and the importance of computational approaches to define spatially distinct regions within the TME.

Spatial analysis revealed distinct differences between spatial count and LDA in how cells were grouped into RCNs, with both methods being sensitive to the chosen radius and the underlying cell size. Spatial count excelled at detecting small, well-defined structures, such as TLSs. However, it also demonstrated high sensitivity to spatial scale, while smaller radii preserved fine-grained distinctions, larger radii led to the convergence especially of immune-related RCNs, highlighting the importance of carefully selecting the radius.

In contrast, LDA generated more stable and homogeneous RCNs across spatial scales, consistently identifying immune compartments even as the radius increased. This robustness reflects LDA's ability to capture smoothly transitioning microenvironments and preserve coherent patterns, as shown in previous studies (Chen et al., 2020; Nirmal et al., 2022). Such properties make LDA particularly useful for capturing more dispersed immune patterns and maintaining neighborhood coherence in the TME.

Notably, most structural changes of RCNs occurred between the 13-25 μm radii, suggesting that RCN structures become more similar and less distinct as the radius increases. Another noteworthy finding was that at the largest spatial radius (35 μm), the clearest distinctions between long and short PFS groups emerged. Patients with short PFS exhibited increased enrichment of stromal neighborhoods, suggesting that stromal expansion is associated with poorer prognosis. This aligns with previous studies showing that stromal cells are associated with immune exclusion and poor treatment response (Zhang et al., 2011; Zhao et al., 2023), further supporting the diagnostic potential of RCN profiling. Interestingly, at larger radii stromal RCNs that included immune cells were significantly more enriched in short-PFS patients, potentially indicating immune suppression or ineffective infiltration into the tumor area.

Both methods offer distinct insights into the TME, each with its own advantages and limitations (Table 1). Spatial count provides detailed, structure-specific insights but is sensitive to spatial scale and susceptible to noise. In contrast, LDA offers a more robust view across scales and also detects disaggregated structures, such as less common immune cells, though it may abstract regions, potentially reducing interpretability. Choosing the most appropriate spatial method and radius should therefore be hypothesis-driven and carefully considered.

Table 1. Comparison of spatial count and LDA Methods.

Aspect	Spatial count	LDA
Sensitivity to spatial scale	High, RCN composition strongly depends on the chosen radius	Lower, more robust across spatial scales
Interpretability	Straightforward, results derived directly from the neighborhoods matrix	More abstract, motif-based patterns may require additional context
Diversity	High, more heterogenous RCNs	Lower, homogenous RCNs especially at smaller radii
Aggregation pattern	Localized, finds structures like TLSs and blood vessels	Disaggregated, finds more subtle patterns in the TME

This study is not without limitations. The relatively small cohort size increases sensitivity to sample-specific effects especially when comparing clinical groups and poses a risk of overfitting. Larger cohorts would help to validate the generalizability of observed RCN patterns. Additionally, only a limited range of spatial radii was evaluated, which may limit the ability to detect additional spatial patterns and potential structural transitions. However, increasing the radius too much may lead to excessive overlapping between cell neighborhoods, potentially blurring biologically distinct regions. Lastly, phenotyping was affected by challenges that are known to affect highly multiplexed imaging analysis, including signal spillover, intermixed staining patterns, and background fluorescence variability. These issues required careful data processing, the use of multiple markers, and the addition of more classification steps.

Emerging spatial approaches, such as spatial lag models, may offer additional insights by detecting continuous gradients in protein expression across tissues, potentially finding patterns that may be missed by methods like LDA and spatial count (Nirmal et al., 2022). Additionally, the development of semi-automated or AI-driven tools for segmentation and phenotyping, such as Tribus (Kang et al., 2025) and Mesmer (Greenwald et al., 2022), holds potential for improving phenotyping accuracy and reducing user bias. For broader biological interpretation, integrating spatial data with other molecular profiling techniques, such as single-cell RNA sequencing, spatial transcriptomics or genome sequencing, could provide a more comprehensive view of tissue architecture and function. Studies combining such approaches have already shown promising results in identifying clinically relevant spatial patterns in HGSC (Launonen et al., 2024).

In conclusion, this thesis provides a comparative evaluation of spatial count and LDA for profiling the TME in HGSC. Both methods offer complementary strengths, spatial count effectively identifies localized microstructures, while LDA provides a more robust and comprehensive view of spatial organization. The choice of method and parameters should be chosen based on the specific biological question and the spatial resolution needed. Importantly, the study highlights the clinical relevance of spatial profiling, supporting the use of computational tools in translational and diagnostic workflows. Future efforts should aim to refine these methods and integrate them with

other multi-omic data, potentially paving the way for more patient-tailored treatment strategies in HGSC.

References

Anderson, N. M., & Simon, M. C. (2020). The tumor microenvironment. *Current Biology*, *30*(16), R921–R925. https://doi.org/10.1016/j.cub.2020.06.081

Angelo, M., Bendall, S. C., Finck, R., Hale, M. B., Hitzman, C., Borowsky, A. D., Levenson, R. M., Lowe, J. B., Liu, S. D., Zhao, S., Natkunam, Y., & Nolan, G. P. (2014). Multiplexed ion beam imaging of human breast tumors. *Nature Medicine*, *20*(4), 436–442. https://doi.org/10.1038/nm.3488

Armstrong, D. K., Alvarez, R. D., Bakkum-Gamez, J. N., Barroilhet, L., Behbakht, K., Berchuck, A., Chen, L., Cristea, M., DeRosa, M., Eisenhauer, E. L., Gershenson, D. M., Gray, H. J., Grisham, R., Hakam, A., Jain, A., Karam, A., Konecny, G. E., Leath, C. A., Liu, J., … Engh, A. M. (2021). Ovarian Cancer, Version 2.2020, NCCN Clinical Practice Guidelines in Oncology. *Journal of the National Comprehensive Cancer Network*, *19*(2), 191–226. https://doi.org/10.6004/jnccn.2021.0007

Arvai, K. (2020). *Kneed* (Version 0.7.0) [Computer software]. https://github.com/arvkevi/kneed

Baker, G. J., Novikov, E., Zhao, Z., Vallius, T., Davis, J. A., Lin, J.-R., Muhlich, J. L., Mittendorf, E. A., Santagata, S., Guerriero, J. L., & Sorger, P. K. (2024). Quality control for single-cell analysis of high-plex tissue profiles using CyLinter. *Nature Methods*, *21*(12), 2248–2259. https://doi.org/10.1038/s41592-024-02328-0

Bengfort, B., & Bilbro, R. (2017). *Yellowbrick* (Version 0.5) [Computer software]. http://www.scikit-yb.org/

Bowtell, D. D., Böhm, S., Ahmed, A. A., Aspuria, P.-J., Bast, R. C., Beral, V., Berek, J. S., Birrer, M. J., Blagden, S., Bookman, M. A., Brenton, J. D., Chiappinelli, K. B., Martins, F. C., Coukos, G., Drapkin, R., Edmondson, R., Fotopoulou, C., Gabra, H., Galon, J., … Balkwill, F. R. (2015). Rethinking ovarian cancer II: Reducing mortality from high-grade serous ovarian cancer. *Nature Reviews Cancer*, *15*(11), 668–679. https://doi.org/10.1038/nrc4019

Burger, R. A., Brady, M. F., Bookman, M. A., Fleming, G. F., Monk, B. J., Huang, H., Mannel, R. S., Homesley, H. D., Fowler, J., Greer, B. E., Boente, M., Birrer, M. J., & Liang, S. X. (2012). Incorporation of Bevacizumab in the Primary Treatment of Ovarian Cancer. *Obstetrical & Gynecological Survey*, *67*(5), 289. https://doi.org/10.1097/OGX.0b013e3182547170

Chen, Z., Soifer, I., Hilton, H., Keren, L., & Jojic, V. (2020). Modeling Multiplexed Images with *Spatial-LDA* Reveals Novel Tissue Microenvironments. *Journal of Computational Biology*, *27*(8), 1204–1218. https://doi.org/10.1089/cmb.2019.0340

Cordani, N., Bianchi, T., Ammoni, L. C., Cortinovis, D. L., Cazzaniga, M. E., Lissoni, A. A., Landoni, F., & Canova, S. (2023). An Overview of PARP Resistance in Ovarian Cancer from a Molecular and Clinical Perspective. *International Journal of Molecular Sciences*, *24*(15), Article 15. https://doi.org/10.3390/ijms241511890

Curiel, T. J., Coukos, G., Zou, L., Alvarez, X., Cheng, P., Mottram, P., Evdemon-Hogan, M., Conejo-Garcia, J. R., Zhang, L., Burow, M., Zhu, Y., Wei, S., Kryczek, I., Daniel, B., Gordon, A., Myers, L., Lackner, A., Disis, M. L., Knutson, K. L., … Zou, W. (2004). Specific recruitment of regulatory T cells in ovarian carcinoma fosters immune privilege and predicts reduced survival. *Nature Medicine*, *10*(9), 942–949. https://doi.org/10.1038/nm1093

Dhatchinamoorthy, K., Colbert, J. D., & Rock, K. L. (2021). Cancer Immune Evasion Through Loss of MHC Class I Antigen Presentation. *Frontiers in Immunology*, *12*. https://doi.org/10.3389/fimmu.2021.636568

Drakes, M. L., & Stiff, P. J. (2018). Regulation of Ovarian Cancer Prognosis by Immune Cells in the Tumor Microenvironment. *Cancers*, *10*(9), Article 9. https://doi.org/10.3390/cancers10090302

Elhanani, O., Ben-Uri, R., & Keren, L. (2023). Spatial profiling technologies illuminate the tumor microenvironment. *Cancer Cell*, *41*(3), 404–420. https://doi.org/10.1016/j.ccell.2023.01.010

Fu, T., Dai, L.-J., Wu, S.-Y., Xiao, Y., Ma, D., Jiang, Y.-Z., & Shao, Z.-M. (2021). Spatial architecture of the immune microenvironment orchestrates tumor immunity and therapeutic response. *Journal of Hematology & Oncology*, *14*(1), 98. https://doi.org/10.1186/s13045-021-01103-4

Fu, Y., Jung, A. W., Torne, R. V., Gonzalez, S., Vöhringer, H., Shmatko, A., Yates, L. R., Jimenez-Linan, M., Moore, L., & Gerstung, M. (2020). Pan-cancer computational histopathology reveals mutations, tumor composition and prognosis. *Nature Cancer*, *1*(8), 800–810. https://doi.org/10.1038/s43018-020-0085-8

Galassi, C., Chan, T. A., Vitale, I., & Galluzzi, L. (2024). The hallmarks of cancer immune evasion. *Cancer Cell*, *42*(11), 1825–1863. https://doi.org/10.1016/j.ccell.2024.09.010

Ghisoni, E., Morotti, M., Sarivalasis, A., Grimm, A. J., Kandalaft, L., Laniti, D. D., & Coukos, G. (2024). Immunotherapy for ovarian cancer: Towards a tailored immunophenotype-based approach. *Nature Reviews Clinical Oncology*, *21*(11), 801–817. https://doi.org/10.1038/s41571-024-00937-4

Goltsev, Y., Samusik, N., Kennedy-Darling, J., Bhate, S., Hale, M., Vazquez, G., Black, S., & Nolan, G. P. (2018). Deep Profiling of Mouse Splenic Architecture with CODEX Multiplexed Imaging. *Cell*, *174*(4), 968-981.e15. https://doi.org/10.1016/j.cell.2018.07.010

Greenwald, N. F., Miller, G., Moen, E., Kong, A., Kagel, A., Dougherty, T., Fullaway, C. C., McIntosh, B. J., Leow, K. X., Schwartz, M. S., Pavelchek, C., Cui, S., Camplisson, I., Bar-Tal, O., Singh, J., Fong, M., Chaudhry, G., Abraham, Z., Moseley, J., … Van Valen, D. (2022). Whole-cell segmentation of tissue images with human-level performance using large-scale data annotation and deep learning. *Nature Biotechnology*, *40*(4), 555–565. https://doi.org/10.1038/s41587-021-01094-0

Hansen, J. M., Coleman, R. L., & Sood, A. K. (2016). Targeting the tumour microenvironment in ovarian cancer. *European Journal of Cancer*, *56*, 131–143. https://doi.org/10.1016/j.ejca.2015.12.016

Hinshaw, D. C., & Shevde, L. A. (2019). The Tumor Microenvironment Innately Modulates Cancer Progression. *Cancer Research*, *79*(18), 4557–4566. https://doi.org/10.1158/0008-5472.CAN-18-3962

Integrated Genomic Analyses of Ovarian Carcinoma. (2011). *Nature*, *474*(7353), 609–615. https://doi.org/10.1038/nature10166

Kabala, Z., Bourhafour, M., Chekrine, T., Bouchbika, Z., Benchekroun, N., Jouhadi, H., Tawfiq, N., Badou, A., & Sahraoui, S. (2023). Epithelial Ovarian Cancer: Microenvironment and Immunecheck Point Inhibitors. *European Journal of Medical and Health Sciences*, *5*(5), Article 5. https://doi.org/10.24018/ejmed.2023.5.5.1896

Kang, Z., Szabo, A., Farago, T., Perez-Villatoro, F., Junquera, A., Shah, S., Launonen, I.-M., Anttila, E., Casado, J., Elias, K., Virtanen, A., Haltia, U.-M., & Färkkilä, A. (2025). Tribus: Semi-automated discovery of cell identities and phenotypes from multiplexed imaging and proteomic data. *Bioinformatics*, *41*(3), btaf082. https://doi.org/10.1093/bioinformatics/btaf082

Kroeger, D. R., Milne, K., & Nelson, B. H. (2016). Tumor-Infiltrating Plasma Cells Are Associated with Tertiary Lymphoid Structures, Cytolytic T-Cell Responses, and Superior Prognosis in Ovarian Cancer. *Clinical Cancer Research*, *22*(12), 3005–3015. https://doi.org/10.1158/1078-0432.CCR-15-2762

Kurman, R. J., & Shih, I.-M. (2016). The Dualistic Model of Ovarian Carcinogenesis: Revisited, Revised, and Expanded. *The American Journal of Pathology*, *186*(4), 733–747. https://doi.org/10.1016/j.ajpath.2015.11.011

Launonen, I.-M., Lyytikäinen, N., Casado, J., Anttila, E. A., Szabó, A., Haltia, U.-M., Jacobson, C. A., Lin, J. R., Maliga, Z., Howitt, B. E., Strickland, K. C., Santagata, S., Elias, K., D'Andrea, A. D., Konstantinopoulos, P. A., Sorger, P. K., & Färkkilä, A. (2022). Single-cell tumor-immune microenvironment of BRCA1/2 mutated high-grade serous ovarian cancer. *Nature Communications*, *13*(1), 835. https://doi.org/10.1038/s41467-022-28389-3

Launonen, I.-M., Niemiec, I., Hincapié-Otero, M., Erkan, E. P., Junquera, A., Afenteva, D., Falco, M. M., Liang, Z., Salko, M., Chamchougia, F., Szabo, A., Perez-Villatoro, F., Li, Y., Micoli, G., Nagaraj, A., Haltia, U.-M., Kahelin, E., Oikkonen, J., Hynninen, J., … Färkkilä, A. (2024). Chemotherapy induces myeloid-driven spatially confined T cell exhaustion in ovarian cancer. *Cancer Cell*, *42*(12), 2045-2063.e10. https://doi.org/10.1016/j.ccell.2024.11.005

Ledermann, J., Harter, P., Gourley, C., Friedlander, M., Vergote, I., Rustin, G., Scott, C., Meier, W., Shapira-Frommer, R., Safra, T., Matei, D., Macpherson, E., Watkins, C., Carmichael, J., & Matulonis, U. (2012). Olaparib Maintenance Therapy in Platinum-Sensitive Relapsed Ovarian Cancer. *New England Journal of Medicine*, *366*(15), 1382–1392. https://doi.org/10.1056/NEJMoa1105535

Lin, J.-R., Izar, B., Wang, S., Yapp, C., Mei, S., Shah, P. M., Santagata, S., & Sorger, P. K. (2018). Highly multiplexed immunofluorescence imaging of human tissues and tumors using t-CyCIF and conventional optical microscopes. *eLife*, *7*, e31657. https://doi.org/10.7554/eLife.31657

Lisio, M.-A., Fu, L., Goyeneche, A., Gao, Z., & Telleria, C. (2019). High-Grade Serous Ovarian Cancer: Basic Sciences, Clinical and Therapeutic Standpoints. *International Journal of Molecular Sciences*, *20*(4), Article 4. https://doi.org/10.3390/ijms20040952

Liu, D., Lin, J.-R., Robitschek, E. J., Kasumova, G. G., Heyde, A., Shi, A., Kraya, A., Zhang, G., Moll, T., Frederick, D. T., Chen, Y.-A., Wang, S., Schapiro, D., Ho, L.-L., Bi, K., Sahu, A., Mei, S., Miao, B., Sharova, T., … Boland, G. M. (2021). Evolution of delayed resistance to immunotherapy in a melanoma responder. *Nature Medicine*, *27*(6), 985–992. https://doi.org/10.1038/s41591-021-01331-8

Lorusso, D., Ceni, V., Daniele, G., Salutari, V., Pietragalla, A., Muratore, M., Nero, C., Ciccarone, F., & Scambia, G. (2020). Newly diagnosed ovarian cancer: Which first-line treatment? *Cancer Treatment Reviews*, *91*, 102111. https://doi.org/10.1016/j.ctrv.2020.102111

Matulonis, U. A., Sood, A. K., Fallowfield, L., Howitt, B. E., Sehouli, J., & Karlan, B. Y. (2016). Ovarian cancer. *Nature Reviews. Disease Primers*, *2*, 16061. https://doi.org/10.1038/nrdp.2016.61

Momenimovahed, Z., Tiznobaik, A., Taheri, S., & Salehiniya, H. (2019). Ovarian cancer in the world: Epidemiology and risk factors. *International Journal of Women's Health*, *11*, 287–299. https://doi.org/10.2147/IJWH.S197604

Muhlich, J. L., Chen, Y.-A., Yapp, C., Russell, D., Santagata, S., & Sorger, P. K. (2022). Stitching and registering highly multiplexed whole-slide images of tissues and tumors using ASHLAR. *Bioinformatics*, *38*(19), 4613–4621. https://doi.org/10.1093/bioinformatics/btac544

Munasarjasyöpä. (n.d.). Kaikki syövästä. Retrieved 15 August 2024, from https://kaikkisyovasta.fi/tietoa-syovasta/syopataudit/munasarjasyopa/

Nirmal, A. J., Maliga, Z., Vallius, T., Quattrochi, B., Chen, A. A., Jacobson, C. A., Pelletier, R. J., Yapp, C., Arias-Camison, R., Chen, Y.-A., Lian, C. G., Murphy, G. F., Santagata, S., & Sorger, P. K. (2022). The Spatial Landscape of Progression and Immunoediting in Primary Melanoma at Single-Cell Resolution. *Cancer Discovery*, *12*(6), 1518–1541. https://doi.org/10.1158/2159-8290.CD-21-1357

Nirmal, A. J., & Sorger, P. K. (2024). SCIMAP: A Python Toolkit for Integrated Spatial Analysis of Multiplexed Imaging Data. *Journal of Open Source Software*, *9*(97), 6604. https://doi.org/10.21105/joss.06604

Nishida, N., Yano, H., Nishida, T., Kamura, T., & Kojiro, M. (2006). Angiogenesis in Cancer. *Vascular Health and Risk Management*, *2*(3), 213–219. https://doi.org/10.2147/vhrm.s23213

O'Connor, M. J. (2015). Targeting the DNA Damage Response in Cancer. *Molecular Cell*, *60*(4), 547–560. https://doi.org/10.1016/j.molcel.2015.10.040

Oza, A. M., Cook, A. D., Pfisterer, J., Embleton, A., Ledermann, J. A., Pujade-Lauraine, E., Kristensen, G., Carey, M. S., Beale, P., Cervantes, A., Park-Simon, T.-W., Rustin, G., Joly, F., Mirza, M. R., Plante, M., Quinn, M., Poveda, A., Jayson, G. C., Stark, D., …

Perren, T. J. (2015). Standard chemotherapy with or without bevacizumab for women with newly diagnosed ovarian cancer (ICON7): Overall survival results of a phase 3 randomised trial. *The Lancet Oncology*, *16*(8), 928–936. https://doi.org/10.1016/S1470-2045(15)00086-8

Pujade-Lauraine, E., Ledermann, J. A., Selle, F., Gebski, V., Penson, R. T., Oza, A. M., Korach, J., Huzarski, T., Poveda, A., Pignata, S., Friedlander, M., Colombo, N., Harter, P., Fujiwara, K., Ray-Coquard, I., Banerjee, S., Liu, J., Lowe, E. S., Bloomfield, R., … Vergote, I. (2017). Olaparib tablets as maintenance therapy in patients with platinum-sensitive, relapsed ovarian cancer and a BRCA1/2 mutation (SOLO2/ENGOT-Ov21): A double-blind, randomised, placebo-controlled, phase 3 trial. *The Lancet Oncology*, *18*(9), 1274–1284. https://doi.org/10.1016/S1470-2045(17)30469-2

Roberts, C. M., Cardenas, C., & Tedja, R. (2019). The Role of Intra-Tumoral Heterogeneity and Its Clinical Relevance in Epithelial Ovarian Cancer Recurrence and Metastasis. *Cancers*, *11*(8), Article 8. https://doi.org/10.3390/cancers11081083

Rodriguez, G. M., Galpin, K. J. C., McCloskey, C. W., & Vanderhyden, B. C. (2018). The Tumor Microenvironment of Epithelial Ovarian Cancer and Its Influence on Response to Immunotherapy. *Cancers*, *10*(8), Article 8. https://doi.org/10.3390/cancers10080242

Saleh, R., & Elkord, E. (2020a). Acquired resistance to cancer immunotherapy: Role of tumor-mediated immunosuppression. *Seminars in Cancer Biology*, *65*, 13–27. https://doi.org/10.1016/j.semcancer.2019.07.017

Saleh, R., & Elkord, E. (2020b). FoxP3+ T regulatory cells in cancer: Prognostic biomarkers and therapeutic targets. *Cancer Letters*, *490*, 174–185. https://doi.org/10.1016/j.canlet.2020.07.022

Santoiemma, P. P., & Powell, D. J. (2015). Tumor infiltrating lymphocytes in ovarian cancer. *Cancer Biology & Therapy*, *16*(6), 807–820. https://doi.org/10.1080/15384047.2015.1040960

Sato, E., Olson, S. H., Ahn, J., Bundy, B., Nishikawa, H., Qian, F., Jungbluth, A. A., Frosina, D., Gnjatic, S., Ambrosone, C., Kepner, J., Odunsi, T., Ritter, G., Lele, S., Chen, Y.-T., Ohtani, H., Old, L. J., & Odunsi, K. (2005). Intraepithelial CD8+ tumor-infiltrating lymphocytes and a high CD8+/regulatory T cell ratio are associated with favorable prognosis in ovarian cancer. *Proceedings of the National Academy of Sciences*, *102*(51), 18538–18543. https://doi.org/10.1073/pnas.0509182102

Sharonov, G. V., Serebrovskaya, E. O., Yuzhakova, D. V., Britanova, O. V., & Chudakov, D. M. (2020). B cells, plasma cells and antibody repertoires in the tumour microenvironment. *Nature Reviews Immunology*, *20*(5), 294–307. https://doi.org/10.1038/s41577-019-0257-x

Sofroniew, N., Lambert, T., Bokota, G., Nunez-Iglesias, J., Sobolewski, P., Sweet, A., Gaifas, L., Evans, K., Burt, A., Doncila Pop, D., Yamauchi, K., Weber Mendonça, M., Buckley, G., Vierdag, W.-M., Royer, L., Can Solak, A., Harrington, K. I. S., Ahlers, J., Althviz Moré, D., … Zhao, R. (2025). *napari: A multi-dimensional image viewer for Python* (Version v0.5.6) [Computer software]. Zenodo. https://doi.org/10.5281/zenodo.14719463

Speiser, D. E., Chijioke, O., Schaeuble, K., & Münz, C. (2023). CD4+ T cells in cancer. *Nature Cancer*, *4*(3), 317–329. https://doi.org/10.1038/s43018-023-00521-2

St Laurent, J., & Liu, J. F. (2024). Treatment Approaches for Platinum-Resistant Ovarian Cancer. *Journal of Clinical Oncology*, *42*(2), 127–133. https://doi.org/10.1200/JCO.23.01771

Stur, E., Corvigno, S., Xu, M., Chen, K., Tan, Y., Lee, S., Liu, J., Ricco, E., Kraushaar, D., Castro, P., Zhang, J., & Sood, A. K. (2022). Spatially resolved transcriptomics of high-grade serous ovarian carcinoma. *iScience*, *25*(3). https://doi.org/10.1016/j.isci.2022.103923

Toninelli, M., Rossetti, G., & Pagani, M. (2023). Charting the tumor microenvironment with spatial profiling technologies. *Trends in Cancer*, *9*(12), 1085–1096. https://doi.org/10.1016/j.trecan.2023.08.004

Tsujikawa, T., Kumar, S., Borkar, R. N., Azimi, V., Thibault, G., Chang, Y. H., Balter, A., Kawashima, R., Choe, G., Sauer, D., El Rassi, E., Clayburgh, D. R., Kulesz-Martin, M. F., Lutz, E. R., Zheng, L., Jaffee, E. M., Leyshock, P., Margolin, A. A., Mori, M., … Coussens, L. M. (2017). Quantitative multiplex immunohistochemistry reveals myeloid-inflamed tumor-immune complexity associated with poor prognosis. *Cell Reports*, *19*(1), 203–217. https://doi.org/10.1016/j.celrep.2017.03.037

Visser, K. E. de, & Joyce, J. A. (2023). The evolving tumor microenvironment: From cancer initiation to metastatic outgrowth. *Cancer Cell*, *41*(3), 374–403. https://doi.org/10.1016/j.ccell.2023.02.016

Weigert, M., Schmidt, U., Haase, R., Sugawara, K., & Myers, G. (2020). Star-convex Polyhedra for 3D Object Detection and Segmentation in Microscopy. *2020 IEEE Winter Conference on Applications of Computer Vision (WACV)*, 3655–3662. https://doi.org/10.1109/WACV45572.2020.9093435

Xu, Y., Zhang, H., Huang, Y., Rui, X., & Zheng, F. (2017). Role of TIM-3 in ovarian cancer. *Clinical and Translational Oncology*, *19*(9), 1079–1083. https://doi.org/10.1007/s12094-017-1656-8

Xue, J., Schmidt, S. V., Sander, J., Draffehn, A., Krebs, W., Quester, I., De Nardo, D., Gohel, T. D., Emde, M., Schmidleithner, L., Ganesan, H., Nino-Castro, A., Mallmann, M. R., Labzin, L., Theis, H., Kraut, M., Beyer, M., Latz, E., Freeman, T. C., … Schultze, J. L. (2014). Transcriptome-Based Network Analysis Reveals a Spectrum Model of Human Macrophage Activation. *Immunity*, *40*(2), 274–288. https://doi.org/10.1016/j.immuni.2014.01.006

Yin, M., Shen, J., Yu, S., Fei, J., Zhu, X., Zhao, J., Zhai, L., Sadhukhan, A., & Zhou, J. (2019). Tumor-Associated Macrophages (TAMs): A Critical Activator In Ovarian Cancer Metastasis. *OncoTargets and Therapy*, *12*, 8687–8699. https://doi.org/10.2147/OTT.S216355

Zhang, Y., Tang, H., Cai, J., Zhang, T., Guo, J., Feng, D., & Wang, Z. (2011). Ovarian cancer-associated fibroblasts contribute to epithelial ovarian carcinoma metastasis by

promoting angiogenesis, lymphangiogenesis and tumor cell invasion. *Cancer Letters*, *303*(1), 47–55. https://doi.org/10.1016/j.canlet.2011.01.011

Zhao, Y., Shen, M., Wu, L., Yang, H., Yao, Y., Yang, Q., Du, J., Liu, L., Li, Y., & Bai, Y. (2023). Stromal cells in the tumor microenvironment: Accomplices of tumor progression? *Cell Death & Disease*, *14*(9), 1–24. https://doi.org/10.1038/s41419-023-06110-6

Appendices

Appendix 1 Antibodies' list

Supplementary Table 1. List of antibodies used for tCycIF.

Antibody	Fluorochrome	Company	Catalog number
CyclinE	647	Invitrogen	32-1600
pChk1 (Ser345)	488	CST	2348S
Tcf1	488	CST	6444S
PRb	555	CST	8957S
CyclinB1	647	CST	4118S
CyclinA	488	SantaCruz	sc-271682AF488
CD11c	555	CST	77882BC
p27	647	Santa Cruz Biotechnology	sc-1641 AF647
Vimentin	750	CST	69227S
TIM-3	488	CST	54669S
PanCK	555	eBioscience-Invitrogen	41-9003-82
Wee1	647	Santa Cruz Biotechnology	sc-5285
CD163	488	Abcam	ab218293
CyclinD1	555	Abcam	ab203448
p21	647	CST	8587S
Ph3	488	CST	3465S
CD45	555	RnD systems	FAB1430P
Anti-phospho-Ser/ Thr-Pro MPM-2	647	EMD millipore	16-220
pRPA	488	CST	31912S
pStat1	555	CST	8183S
CD20	647	Abcam	ab288330
PCNA	488	CST	8580S
Geminin	555	Proteintech	CL555-10802-100
gH2Ax	647	BioLegend	613407

CD4	488	RnD systems	FAB8165G
aSMA	555	Abcam	ab202509
CD8a	647	eBioscience-Invitrogen	50-0008-80
Iba1	488	Abcam	ab195031-1001
PAX8		Abcam	ab217733
PD-1	647	Abcam	ab201825
Ki67	488	CST	11882S
FOX-P3	555	eBioscience-Invitrogen	41-4777-80
CD31	647	Abcam	ab218582
FAP	555	Abcam	AB313303
NKG2a	647	Abcam	ab300745

Appendix 2 Elbow plots for spatial count and LDA

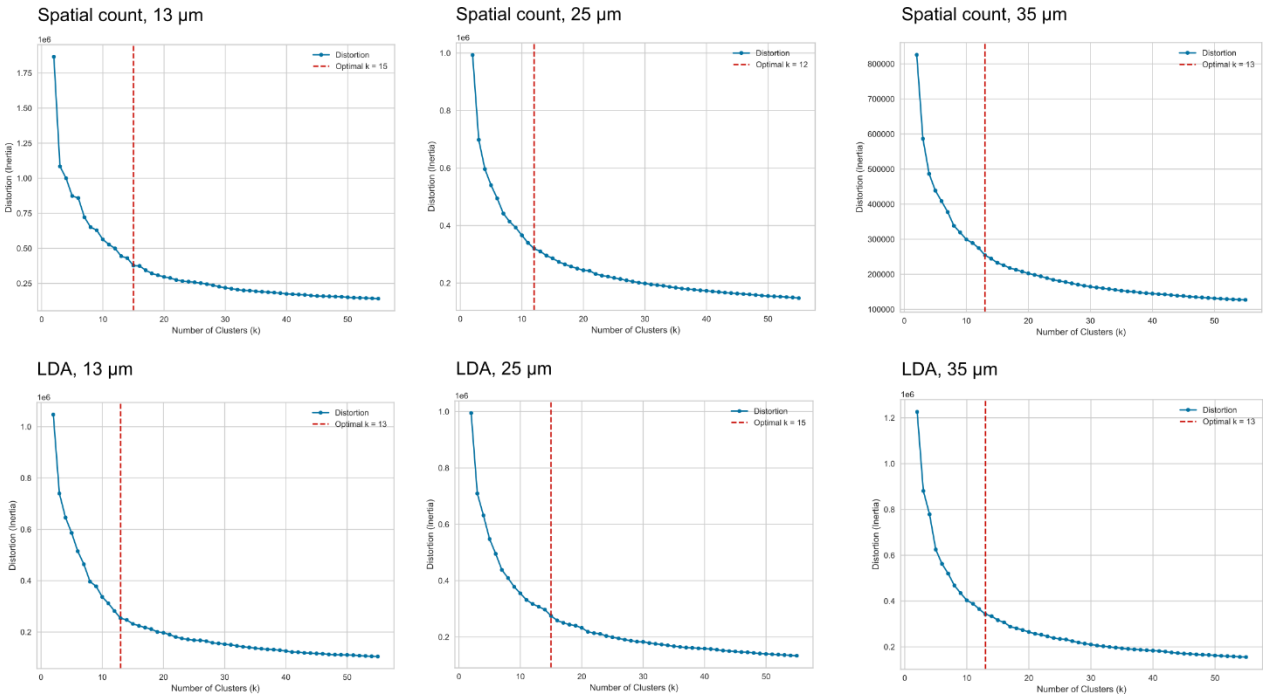

Supplementary Figure 1. Elbow plots showing distortion across cluster numbers for spatial count and LDA at 13, 25, and 35 µm radii. The red dashed lines indicate the selected optimal number of clusters.

Appendix 3 RCN abundances reveal distinct patient clusters

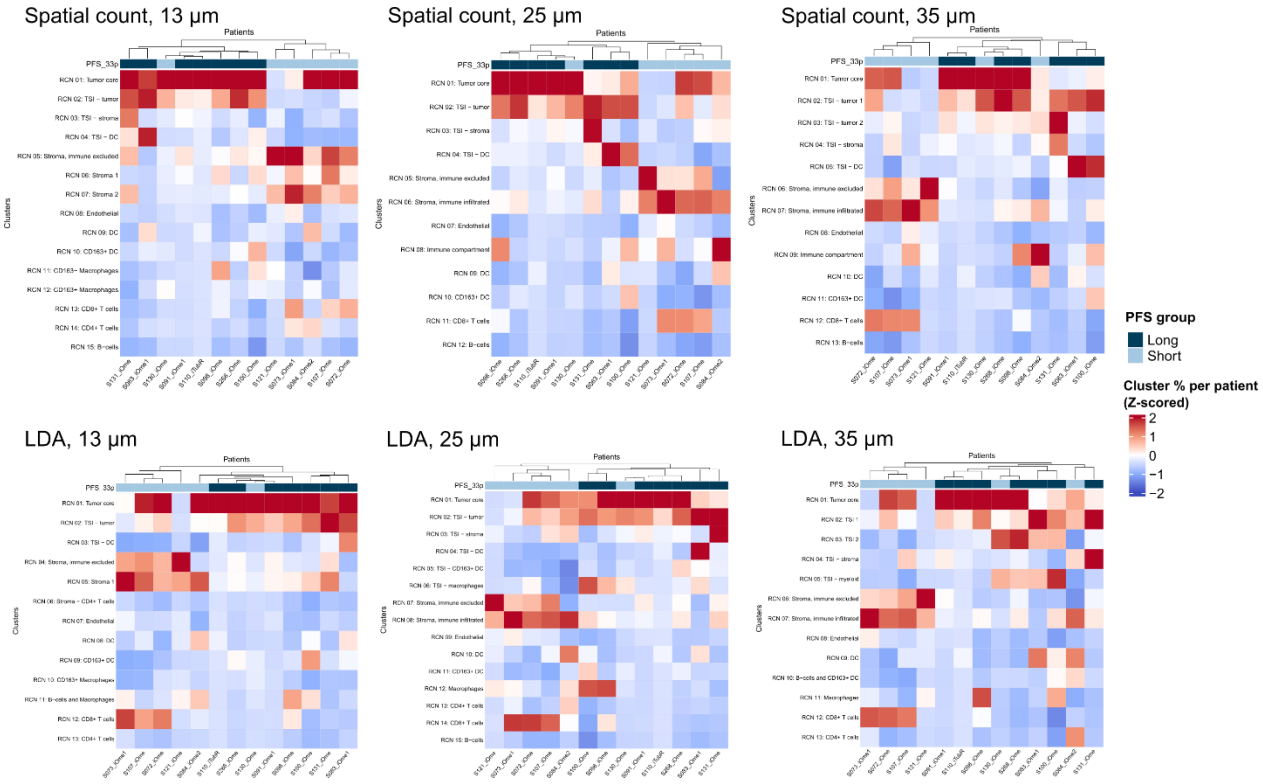

Supplementary Figure 2. Z-scored heatmaps showing hierarchical clustering of relative RCN abundances across patients for spatial count and LDA at 13, 25, and 35 µm radii. The analysis includes patients from the short and long PFS groups.